Journal of Wind Engineering & Industrial Aerodynamics 227 (2022) 105068

Contents lists available at ScienceDirect

Journal of Wind Engineering & Industrial Aerodynamics

journal homepage: www.elsevier.com/locate/jweia

Bridge buffeting by skew winds: A quasi-steady case study

Bernardo Morais da Costa [a,b,*], Jungao Wang [a,b], Jasna Bogunović Jakobsen [a], Ole Andre Øiseth [c], Jónas Þór Snæbjörnsson [a,d]

[a] Department of Mechanical and Structural Engineering and Materials Science, University of Stavanger, Kristine Bonnevies vei 22, 4021, Stavanger, Norway
[b] Norwegian Public Roads Administration, Bergelandsgata 30, 4012, Stavanger, Norway
[c] Department of Structural Engineering, Norwegian University of Science and Technology, Richard Birkelands vei 1A, 7491, Trondheim, Norway
[d] Department of Engineering, Reykjavik University, Menntavegur 1, 102, Reykjavík, Iceland

ARTICLE INFO

Keywords:
Skew wind
Yaw angle
Buffeting response
Bridge aerodynamics
Wind tunnel tests
Aerodynamic coefficients
Floating bridge
Curved bridge
Constrained polynomial regression

ABSTRACT

The buffeting response of a 5000-m-long curved floating bridge is investigated for different mean wind directions, with emphasis on the wind load formulations and use of experimental data. Wind tunnel tests, with a section model of the bridge girder, provided six aerodynamic coefficients for different yaw and inclination angles. A comprehensive 3D buffeting formulation with bivariate polynomial fits of the coefficients is proposed and investigated. For cases where the skew wind data is not available, alternative 2D formulations, including the traditional "cosine rule", are examined. A finite element model is established together with the three-dimensional wind field, in both frequency- and time-domain, and the structural response is analysed. The response is compared for: linear and non-linear coefficient formulations, different buffeting load formulations, different fitting methods, different coefficients considered and different quasi-steady motion-dependent force formulations. The case study demonstrates limitations of the 2D buffeting formulations, in particular of the "cosine rule", and further supports the use of 3D buffeting formulations, the gathering of comprehensive data for skew wind loads and the use of constrained polynomials when fitting and extrapolating the data. This study also provides valuable insight on how to perform these analyses and overcome some of the practical challenges.

1. Introduction

The Norwegian Parliament has a long-term plan to develop and improve the E39 Coastal Highway Route, outlined in Fig. 1 (Samferdselsdepartement, 2017). Within this plan lies the stretch between the cities of Stavanger and Bergen, where a roughly 5-km-long floating bridge is planned to cross the Bjørnafjord. Such a pioneering project comprises many challenges, with the present work focusing on the wind loads and skew wind effects in particular.

Bridges located in steep surroundings are often subject to wind channelling effects, marked by narrow distributions of mean wind directions, which can differ drastically from those observed in nearby offshore measurements. This observation is seen to a different extent in Lysefjord (Cheynet et al., 2020), Hardangerfjord (Castellon et al., 2021), and Sulafjord (Midjiyawa et al., 2021). Contrastingly, near-flat surroundings such as at the Donghai Bridge allow wider and more uniform distributions of mean wind directions (Zhou et al., 2020). Bjørnafjord, shown in Figs. 1 and 2, exhibits topographic effects that lie in-between the examples mentioned, with moderate wind channelling effects and multiple relevant wind directions (Cheynet et al., 2018). The planned bridge deck is curved in the horizontal plane, and it also includes vertical curvatures and slopes. This geometry naturally gives rise to skew winds along most or all of its length. Other motivations to study skew wind effects include e.g. assisting full-scale studies which deal with wind and bridge response data for arbitrary mean wind directions, fatigue analyses which require a comprehensive understanding of the environmental loads, as well as bridge operation and maintenance decision support.

Traditionally, when analysing the buffeting response of a bridge deck, only the wind components perpendicular to the deck are considered and treated as a 2D flow-structure interaction problem in the normal plane, as introduced in (Davenport, 1961a). This formulation, denoted as a 2D approach, can be supplemented with an axially oriented aerodynamic load whenever the bridge is sensitive to axial loads, making it a so-called 2D + 1D approach where 1D represents the axial

* Corresponding author. Department of Mechanical and Structural Engineering and Materials Science, University of Stavanger, Kristine Bonnevies vei 22, 4021, Stavanger, Norway.
E-mail addresses: bercos@vegvesen.no (B. Morais da Costa), jungao.wang@vegvesen.no (J. Wang), jasna.b.jakobsen@uis.no (J.B. Jakobsen), ole.oiseth@ntnu.no (O.A. Øiseth), jonasthor@ru.is (J. Snæbjörnsson).

https://doi.org/10.1016/j.jweia.2022.105068
Received 22 October 2021; Received in revised form 19 May 2022; Accepted 16 June 2022
Available online 2 July 2022

Table of notations

Variables

β	Local mean yaw angle
$\widetilde{\beta}$	Local instantaneous yaw angle (turbulence dependent)
β^*	Smallest angle between the xy-projection of $\boldsymbol{X_u}$ and the y axis
$\beta_{Cardinal}$	Global mean yaw angle, with respect to the wind cardinal directions
β_G	Global mean yaw angle, with respect to the Gs coordinate system
$\beta_{rx=0}$	β before rotating the model test by rx
Δ_i	Displacements in the degree-of-freedom i
$\Delta X_u, \Delta Y_v, \Delta Z_w$	Distance between two reference points, in the $\boldsymbol{X_u}$, $\boldsymbol{Y_v}$ and $\boldsymbol{Z_w}$ directions
θ	Local mean inclination angle
$\widetilde{\theta}$	Local instantaneous inclination angle (turbulence dependent)
θ_{yz}, $\widetilde{\theta}_{yz}$	yz-plane projections of θ and $\widetilde{\theta}$
θ_G	Global mean inclination angle
ρ	Air density
σ_{Δ_i}	Standard deviation of the displacements in the i axis
$\boldsymbol{A}$	Matrix dependent on tested β and θ angles such that $\boldsymbol{Ax}$ returns polynomials
A_i	Non-dimensional parameter to regulate the frequency distribution of $i = u, v, w$
$\boldsymbol{b}$	Vector of tested aerodynamic coefficients
B; $\boldsymbol{B}$	Cross-section width; Diagonal matrix: $diag(B,B,B,B^2,B^2B^2)$
c_i	Polynomial coefficients
C_i, $\boldsymbol{C_i}$	Static aerodynamic coefficient in the i axis; Vector of static aerodynamic coefficients in the coordinate system i
$C_i^{'\beta}$	Partial derivative of C_i with respect to β
$C_i^{'\theta}$	Partial derivative of C_i with respect to θ
f	Frequency, in Hertz
$\boldsymbol{f_{mean,i}}$	Vector of mean wind forces, per unit length, in the coordinate system i
H	Cross-section height
I_i	Turbulence intensity of i
$K_{i,j}$	Non-dimensional decay coefficient of the turbulence component i, to decrease coherence along the direction j
L	Bridge element length
L_{i,X_u}	Characteristic length scale of i in the direction of $\boldsymbol{X_u}$
P	Polynomial function
S_i	Auto spectral density of the turbulence component i
S_{ii}, $S_{i_1 i_2}$	Diagonal entry of the cross spectral density matrix of the turbulence component i; Off-diagonal entry of the cross spectral density matrix associated with turbulence components i_1 and i_2
S_{Δ_i}	Auto spectral density of the nodal displacement response in the i axis
$\boldsymbol{T_{sym}}$	Transformation matrix to impose symmetry properties
u	Turbulence component along the mean wind
U, U_i, $\boldsymbol{U}$	Mean wind speed; mean wind projection onto the i axis or i plane; Mean wind vector
$\widetilde{U}$, $\widetilde{U}_i$	Local instantaneous wind speed; local instantaneous wind projection onto the i axis or i plane (both turbulence dependent)
$\boldsymbol{U}_{rx=0}$	Mean wind vector, before rotating the model test by rx
v	Horizontal turbulence component across the mean wind
w	Upward turbulence component, perpendicular to u and v
$\boldsymbol{x}$	Vector of polynomial coefficients

Accents / styles

~	Time-varying quantity due to turbulence
boldface	Variables in **bold** represent vectors and matrices

Acronyms

1D, 2D or 3D	1-, 2-, or 3-dimensional in space
CFD	Computational fluid dynamics
DOF	Degrees-of-freedom
FEM	Finite element method
QS	Quasi-steady

Coordinate systems and respective axes

Gs (X,Y,Z)	Global structural (X,Y,Z,rX,rY,rZ)
Ls (x,y,z)	Local structural (x,y,z,rx,ry,rz)
Gw $(\boldsymbol{X_u},\boldsymbol{Y_v},\boldsymbol{Z_w})$	Global mean wind $(\boldsymbol{X_u},\boldsymbol{Y_v},\boldsymbol{Z_w},\boldsymbol{rX_u},\boldsymbol{rY_v},\boldsymbol{rZ_w})$

Fig. 1. a) E39 Coastal highway route project, Norway. b) One proposed floating bridge solution for the Bjørnafjord, Norway.

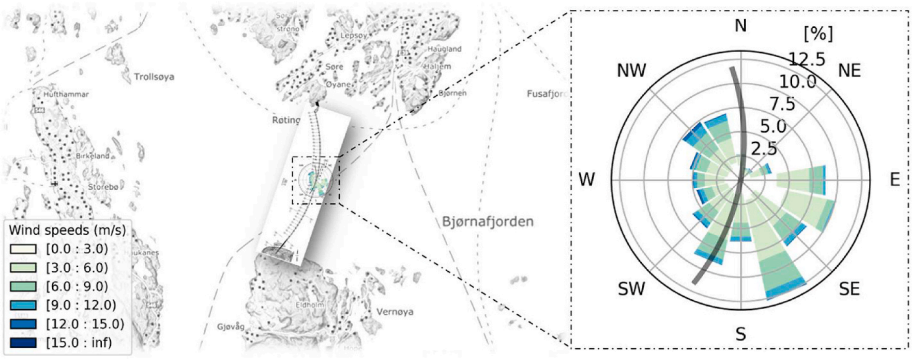

Fig. 2. Wind rose of long-term synthetic data at the centre of the Bjørnafjord (60°06′*N* 5°22′*E*), corrected by nearby wind measurements.

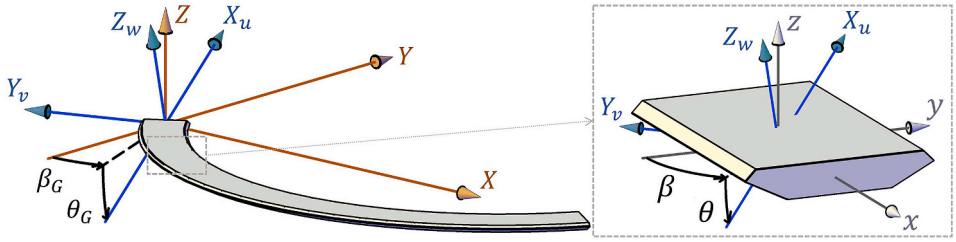

Fig. 3. Global wind – Gw – $(\boldsymbol{X_u}, \boldsymbol{Y_v}, \boldsymbol{Z_w})$ and global structural – Gs – $(\boldsymbol{X}, \boldsymbol{Y}, \boldsymbol{Z})$ coordinate systems; global mean yaw angle β_G and global mean inclination angle θ_G; Global wind – Gw – $(\boldsymbol{X_u}, \boldsymbol{Y_v}, \boldsymbol{Z_w})$ and local structural – Ls – $(\boldsymbol{x}, \boldsymbol{y}, \boldsymbol{z})$ coordinate systems; local mean yaw angle β and local mean inclination angle θ.

Table 1
Input parameters for the wind simulation.

$A_u = 6.8$	$A_v = 9.4$	$A_w = 9.4$
$L_{u,X_u} = 111.8\,m$	$L_{v,X_u} = 27.9\,m$	$L_{w,X_u} = 9.3\,m$
$K_{u,X_u} = 3.0$	$K_{v,X_u} = 6.0$	$K_{w,X_u} = 3.0$
$K_{u,Y_v} = 10.0$	$K_{v,Y_v} = 6.5$	$K_{w,Y_v} = 6.5$
$K_{u,Z_w} = 10.0$	$K_{v,Z_w} = 6.5$	$K_{w,Z_w} = 3.0$
$I_u = 0.137$	$I_v = 0.115$	$I_w = 0.082$
$U = 33.4\,m/s$ $(Z = 14.5\,m)$		

direction, as described in (Costa et al., 2022). When the mean wind is in the same horizontal plane as the bridge girder, these approaches are often simplified into what is generally referred to as the "Cosine rule" or "Cosine + Sine rule" (see e.g. (Tanaka and Davenport, 1982) and (Kimura and Tanaka, 1992) respectively). 2D formulations are the only feasible option when only univariate aerodynamic coefficient functions $C(\theta_{yz})$ are available (here, θ_{yz} is the projection of the inclination angle θ onto the normal yz plane shown in Fig. 3). Such univariate aerodynamic coefficients are often obtained in wind tunnel tests with the deck placed normal to the wind, or through 2D CFD simulations of the deck cross-section.

Literature, however, includes several example cases where the 2D approaches underestimate the bridge buffeting response when compared to measured data. This was observed for example in (Tanaka and Davenport, 1982), (Kimura and Tanaka, 1992), (Zhu and Xu, 2005), (Xu and Zhu, 2005), (Wang et al., 2011), (Huang et al., 2012), (Li et al., 2016) and (Jian et al., 2020). A brief description of each of these literary

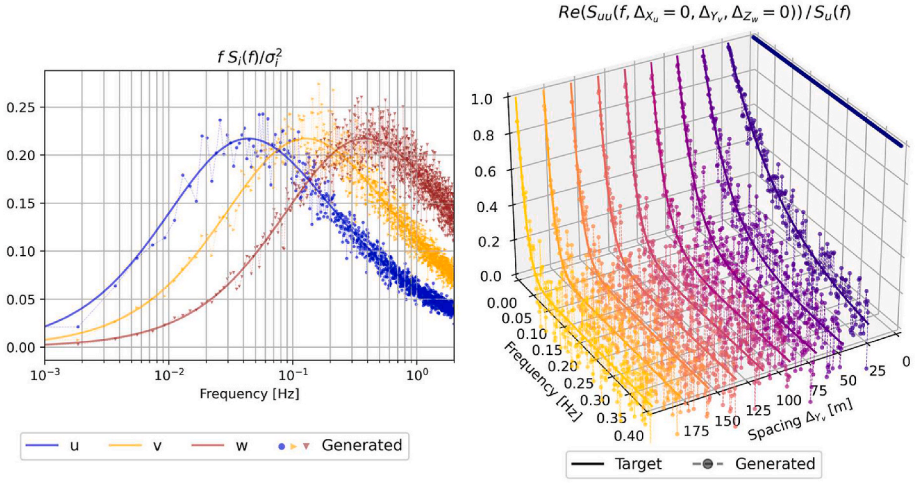

Fig. 4. Comparison between the target and numerically generated values of the normalized auto-spectra of turbulence components and of one normalized co-spectrum of u as a function of the frequency and the distance of two colinear reference points along the $\boldsymbol{Y_v}$ axis, using the parameters from Table 1. Welch's method was used in this figure (with 20 non-overlapping windows) for a better visual comparison.

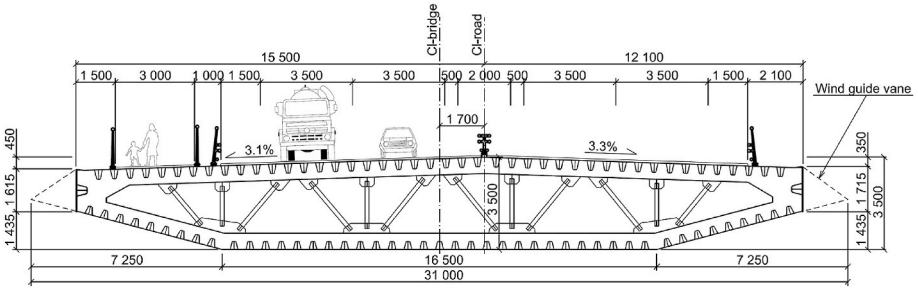

Fig. 5. Cross-section of the bridge girder used for the model test (including the wind guide vanes) [mm].

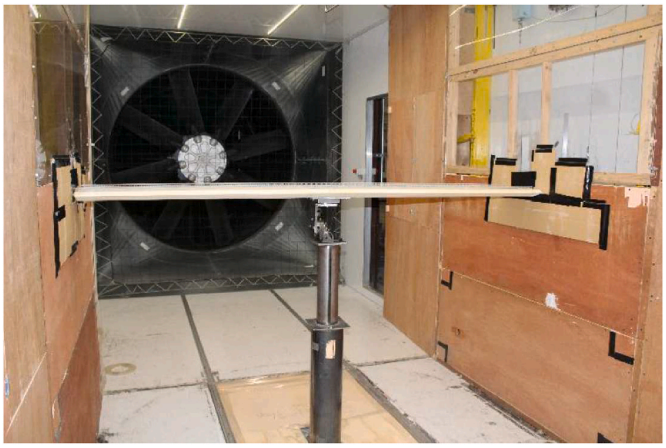

Fig. 6. Model setup for.$(\beta, \theta) = (0°, 0°)$

Fig. 7. Model setup for.$(\beta, \theta) = (50.94°, -1.89°)$

examples was introduced in (Costa et al., 2022) and is not repeated here.

To improve the theoretical buffeting models, a 3D formulation was originally developed in (Zhu, 2002), where bivariate aerodynamic coefficients $C(\beta, \theta)$ are first estimated in a wind tunnel for different combinations of the yaw angle (β) and the inclination angle (θ), and then included in the analysis accordingly. Diverging ratios of aerodynamic coefficients and their respective "Cosine rule" approximations were reported by Zhu, signifying important differences between 2D and 3D approaches. A follow-up work in (Costa et al., 2022), which made further improvements to these approaches, also provides a useful overview of the different theoretical skew wind buffeting models, and is used as the basis for the current case study.

Svend Ole Hansen ApS performed a series of wind tunnel tests on a

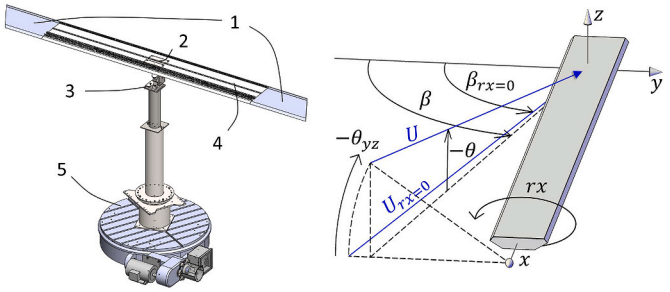

Fig. 8. Model parts: 1) Disconnected pseudo ends; 2) 6 DOF force sensor; 3) rotary joint for *rx*; 4) bridge girder; 5) rotary table for *rZ*; Schematic relation between the rotation *rx*, the mean wind vectors $U_{rx=0}$ (before the rotation) and U, and the angles $\beta_{rx=0}$, β, θ, θ_{yz}.

section model of the bridge girder studied. The gathered data is presented and used in this study. Aerodynamic coefficients at 30 different combinations of β and θ are estimated. Despite obtaining results for β up to 50°, beyond a range previously documented in the literature, significant extrapolations are still necessary for a full description of the buffeting response under skew winds. The challenges of fitting the data and extrapolating the results are carefully presented and discussed. Constrained polynomial fits are proposed and compared with their unconstrained counterparts. A comparison is made between the univariate polynomial fits that do not consider the skew wind data at $\beta \neq 0°$ and the bivariate polynomial fits that consider all the data. The traditional "Cosine rule" extrapolation is also included for comparison.

A finite element model is developed exclusively in *Python*, together with the different theoretical buffeting models. Buffeting analyses are conducted and compared in both frequency- and time-domain. Analyses that use non-linear aerodynamic coefficients are compared with their linearized counterparts. The different skew wind formulations, namely 2D, 2D + 1D and 3D, and the different fitting methods are compared in terms of bridge response. Finally, the effects of the quasi-steady motion-dependent forces are assessed, using the formulation presented in (Zhu, 2002) as well as the main and alternative formulations presented in (Costa et al., 2022).

2. Case study: A curved floating bridge in Bjørnafjorden

The bridge considered in this study is one of four proposed alternatives to cross the Bjørnafjord in Norway. Three floating bridge alternatives with several pontoons moored to the seabed, and one alternative without any mooring lines, have been proposed (Norwegian Public Roads Administration, 2019a) (Norwegian Public Roads Administration, 2019b). Any one of these alternatives promises to extend the current longest floating bridge record, from 2350 m (White, 2013) to roughly 5000 m. The case studied herein is the alternative without mooring lines, which owes its horizontal stiffness to its curvature, with a horizontal radius of also 5000 m. This unprecedently long and unique

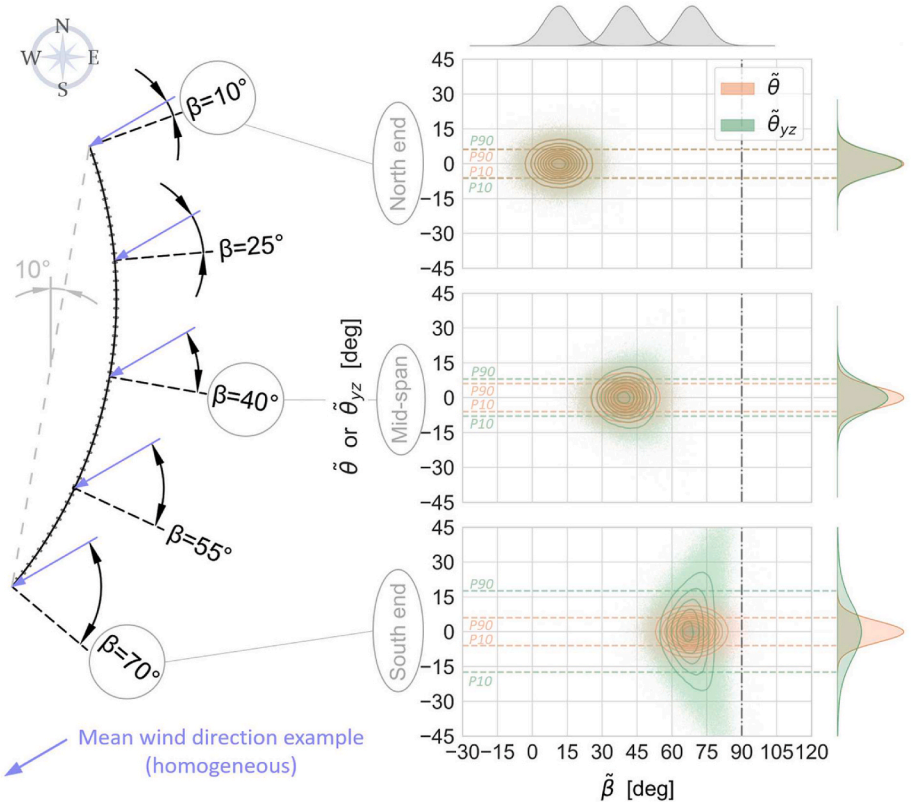

Fig. 9. Left: Example of one homogeneous mean wind direction and associated local mean yaw angles β along the curved floating bridge. Right: Joint and marginal probability density functions of the instantaneous yaw and inclination angles, $\tilde{\beta}$ and $\tilde{\theta}$, due to turbulence, at three different bridge nodes. The yz-plane projection of inclination angle, $\tilde{\theta}_{yz}$, is also included for reference.

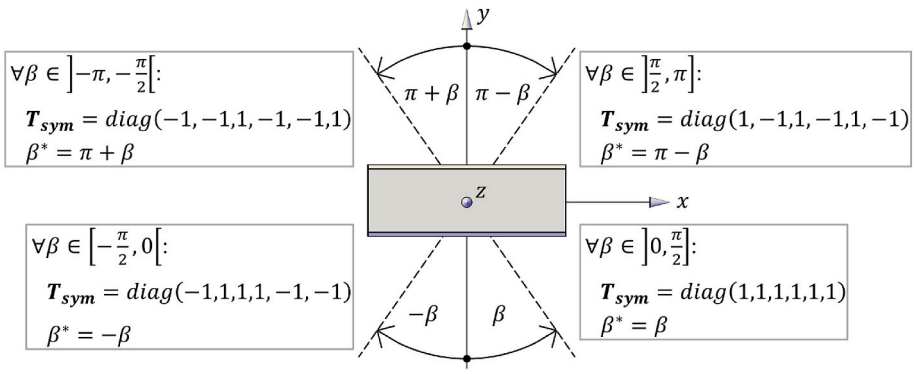

Fig. 10. Values of $\boldsymbol{T_{sym}}$ and β^* to be used in eq. (14), for different β-intervals, to impose symmetry from the tested domain $\beta \in [0°, 90°]$ to the domain $\beta \in]-180°, 180°]$, assuming a vertical xz plane of symmetry.

structure is fixed at both ends and will be subject to various environmental loads.

The coordinate systems used and referred to hereafter are shown in Fig. 3, where the global wind axes $\boldsymbol{X_u}$, $\boldsymbol{Y_v}$ and $\boldsymbol{Z_w}$ coincide with the directions of u, v and w, respectively, which are the three wind turbulence components, namely the along-wind, the horizontal across-wind and the remaining upward orthogonal component. $\boldsymbol{X}$, $\boldsymbol{Y}$, $\boldsymbol{Z}$ and $\boldsymbol{x}$, $\boldsymbol{y}$, $\boldsymbol{z}$ are the global and local structural axes, respectively.

2.1. Wind characteristics

The wind field is, for the sake of simplicity, considered a stationary, homogenous stochastic process with equal velocity, turbulence, and coherence properties, for all mean wind directions. This simplification isolates the effect of the wind direction on the bridge aerodynamics and the resulting structural response. The single-point spectrum used, shown in eq. (1), is given by the Norwegian bridge design manual (Norwegian Public Roads Administration, 2015), which is a "blunt model" (Olesen et al., 1984) inspired by the Kaimal spectrum (Kaimal et al., 1972). The normalized co-spectrum used, whose diagonal and off-diagonal entries are shown in eqs. (2a) and (2b) respectively, is a root sum of squares adaptation of that in (Davenport, 1961b), to consider the three-dimensionality of the wind field. The correlation between different turbulence components was assumed to be zero, to comply with the design manual and for simplicity. However, the effects of a non-zero S_{uw} are potentially relevant, in particular for low natural frequencies, as suggested by (Øiseth et al., 2013) and by another ongoing study. The relevant parameters are summarized in Table 1, for Z =

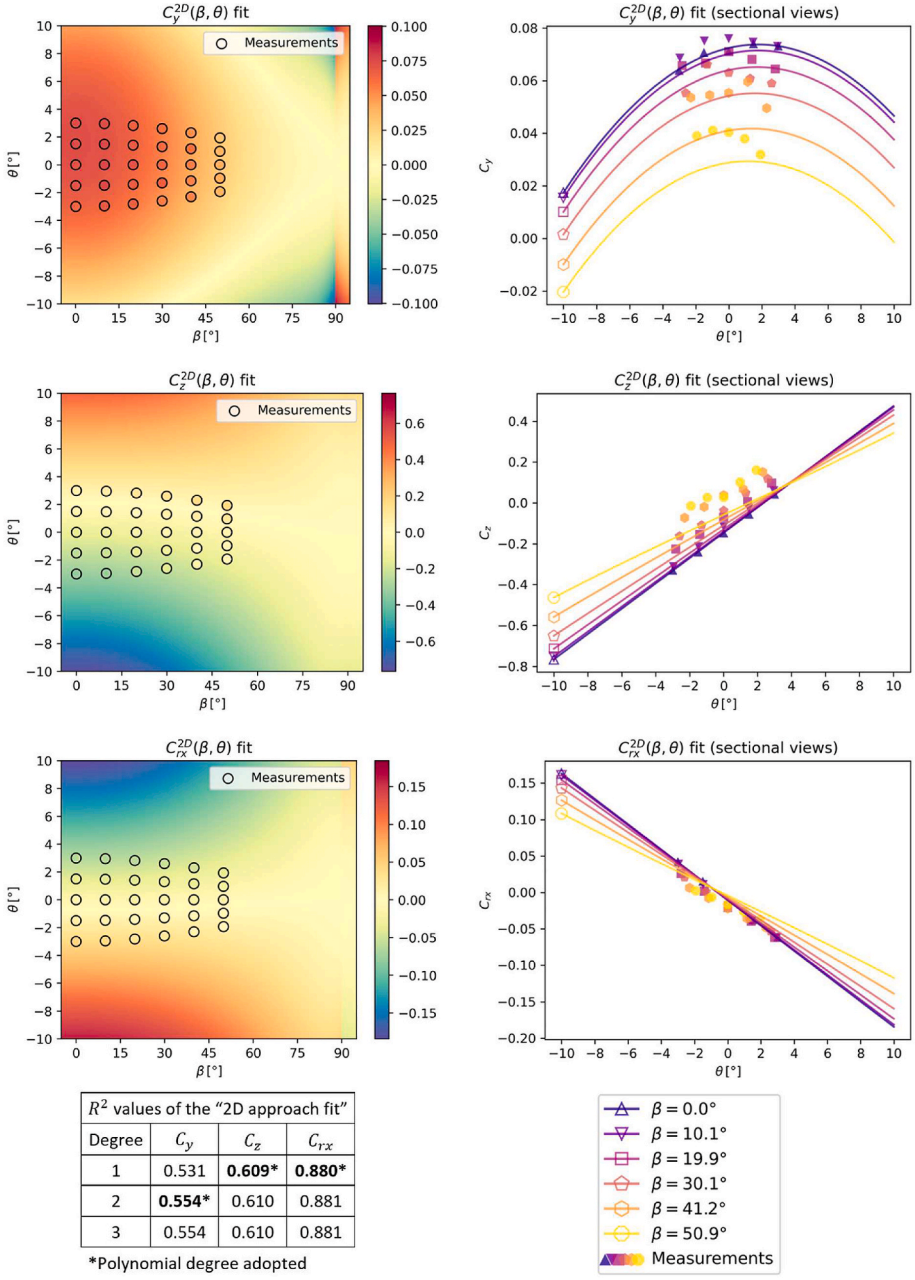

R^2 values of the "2D approach fit"			
Degree	C_y	C_z	C_{rx}
1	0.531	**0.609***	**0.880***
2	**0.554***	0.610	0.881
3	0.554	0.610	0.881

*Polynomial degree adopted

Fig. 11. Comparing the $\boldsymbol{C}^{2D}(\beta,\theta)$ fit with the measurements $\boldsymbol{C}(\beta,\theta)$. The fit was obtained with an n^{th} degree univariate polynomial at $(\beta = 0°, \theta)$ and a 2D approach extrapolation to other β as in eq. (12).

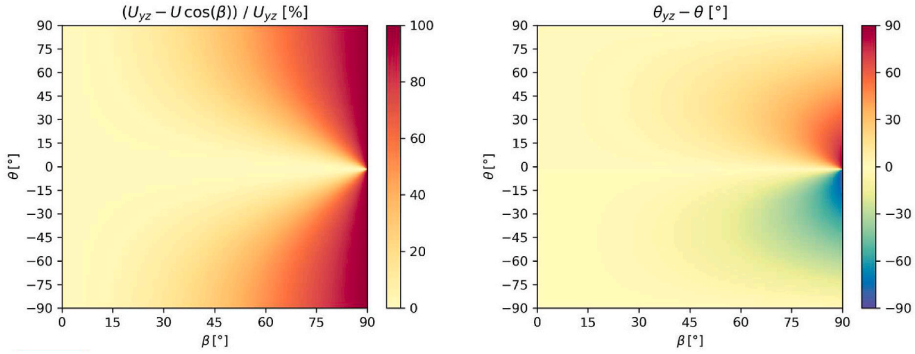

Fig. 12. Assessing the two assumptions of the Cosine rule approximation of the 2D approach, namely that $U_{yz} \approx U\cos\beta$ (left plot) and $\theta_{yz} \approx \theta$ (right plot).

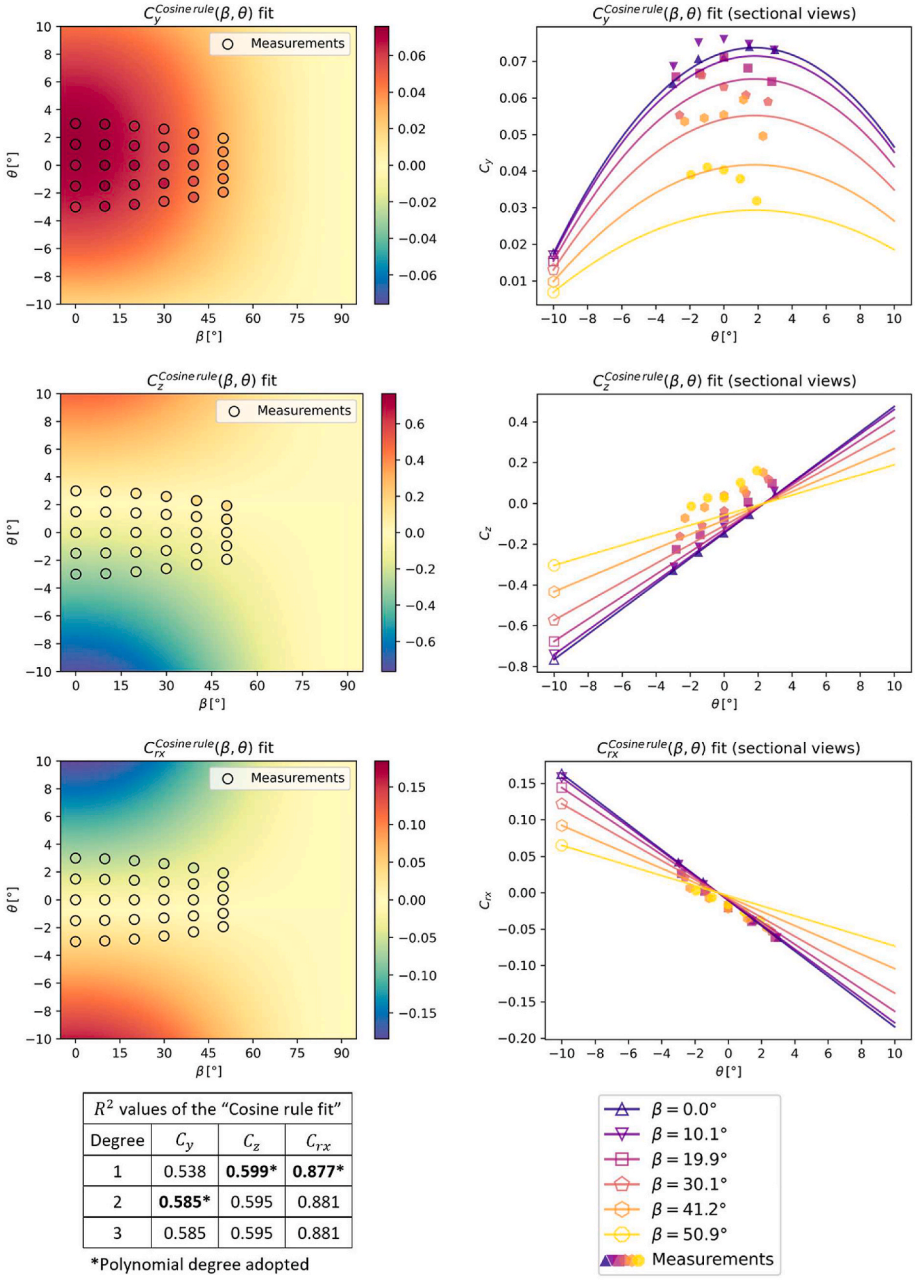

R^2 values of the "Cosine rule fit"			
Degree	C_y	C_z	C_{rx}
1	0.538	**0.599***	**0.877***
2	**0.585***	0.595	0.881
3	0.585	0.595	0.881

*Polynomial degree adopted

Fig. 13. Comparing the $\boldsymbol{C}^{Cosine\ rule}(\beta,\theta)$ fit with the measurements $\boldsymbol{C}(\beta,\theta)$. The fit was obtained with an n^{th} degree univariate polynomial at $(\beta = 0°, \theta)$ and a Cosine rule extrapolation to other β as in eq. (13).

14.5 m (above sea level).

$$\frac{f\,S_i(f)}{\sigma_i^2} = \frac{A_i \widehat{f}_i}{(1+1.5A_i\widehat{f}_i)^{5/3}}\ ;\quad where:\ \widehat{f}_i = \frac{f\,L_{i,X_u}}{U}\ ;\quad for\ i = u,v,w \tag{1}$$

$$\frac{Re(S_{ii}(f,\Delta X_u,\Delta Y_v,\Delta Z_w))}{S_i(f)} = \exp\left(- \sqrt{\left(K_{i,X_u}\frac{f\Delta X_u}{U}\right)^2 + \left(K_{i,Y_v}\frac{f\Delta Y_v}{U}\right)^2 + \left(K_{i,Z_w}\frac{f\Delta Z_w}{U}\right)^2} \right) \tag{2a}$$

$$\frac{Re(S_{i_1 i_2}(f,\Delta X_u,\Delta Y_v,\Delta Z_w))}{\sqrt{S_{i_1}(f)\cdot S_{i_2}(f)}} = 0,\ for\ i,i_1,i_2 = u,v,w\ and\ i_1 \neq i_2 \tag{2b}$$

S_i is the single-point spectrum of the turbulence component i, which is then normalized by the frequency f, in Hertz, and the variance σ_i^2 of the considered turbulence component. A_i is a non-dimensional parameter used to regulate the frequency distribution of the turbulence component i and L_{i,X_u} is its characteristic length scale, in the X_u direction, which is equivalent to its average eddy size. S_{ii} and $S_{i_1 i_2}$ represent the diagonal and off-diagonal entries of the wind co-spectral matrix, respectively. ΔX_u, ΔY_v and ΔZ_w are the distances between two reference points in the Gw (Global wind) coordinate system. $K_{i,j}$ represents the non-dimensional exponential decay coefficient of the turbulent component i, used to decrease its coherence with increasing frequency and increasing distance in the direction $j = X_u, Y_v, Z_w$. The values adopted for each parameter in the case studied are presented in Table 1, where $I_i = \sigma_i/U$ is the turbulence intensity of i. These values were obtained following the latest available version of the project-related design basis (Norwegian Public Roads Administration, 2018), except the three decay coefficients K_{i,X_u} which were taken from an aerodynamic design

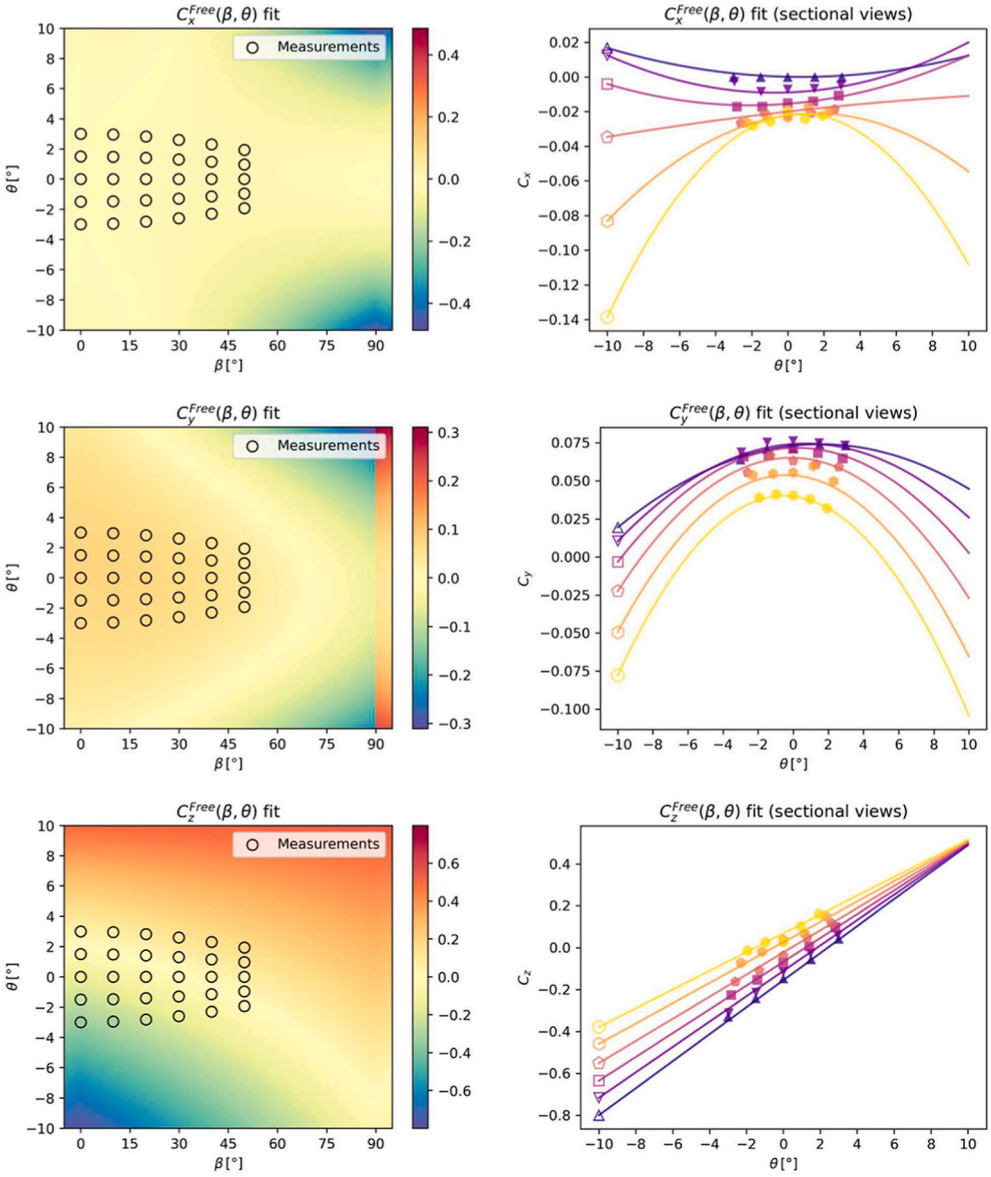

Fig. 14. Free bivariate polynomial fits of the aerodynamic coefficients.

report (Norwegian Public Roads Administration, 2019c).

The wind field can be then generated numerically, through e.g. the procedure shown in (Shinozuka, 1972) and (Deodatis, 1996), and used in time-domain simulations of the response. Various methods to compute the wind field have been proposed, e.g., (Di Paola, 1998; Hémon and Santi, 2003; Tao et al., 2021), with different computational efficiency. The target and the generated non-dimensional auto-spectral densities of each turbulence component, using the parameters from Table 1, are illustrated in Fig. 4 (left-hand plot). The first diagonal entry of the co-spectrum (concerning the u component) is also illustrated in its normalized form and zoomed for the frequencies of interest (right-hand plot). It is a function of the frequency and the vector of distances $(\Delta X_u, \Delta Y_v, \Delta Z_w)$ between the two reference points, which in this example are assumed to be colinear with the Y_v axis for illustration purposes. 3-hour long Monte Carlo simulations of the wind field, with a sampling frequency of 4 Hz, were used. The Welch method, with 20 non-overlapping windows, was used in both plots of Fig. 4 for a better visual comparison (reducing the noise at the cost of lower frequency resolution). The wind simulations for this study were performed in *Python*. A compromise between computational time and accuracy was found by simulating several independent 10-min long "wind blocks". To prevent abrupt changes in the wind velocities, these blocks are concatenated with 8-s-long overlapping periods and a linear transition between velocities of adjacent blocks.

2.2. Wind tunnel experiment

Svend Ole Hansen ApS performed a series of wind tunnel tests in connection with the Bjørnafjord floating bridge project, including static section model tests under skew winds (Norwegian Public Roads Administration, 2019e). The test results and the raw data were provided to the authors and were further examined. The model is 2.40 m long, has a geometric scale of 1:80, and has an aspect ratio of 6.2 (length / width). A straight strip theory is assumed valid due to the large curvature radius of the bridge and the relatively rapid decaying coherence of the wind. The relevant static model setup is described in Fig. 5, Fig. 6, Fig. 7 and Fig. 8.

In a wind tunnel setting it is often practical to perform rotations of

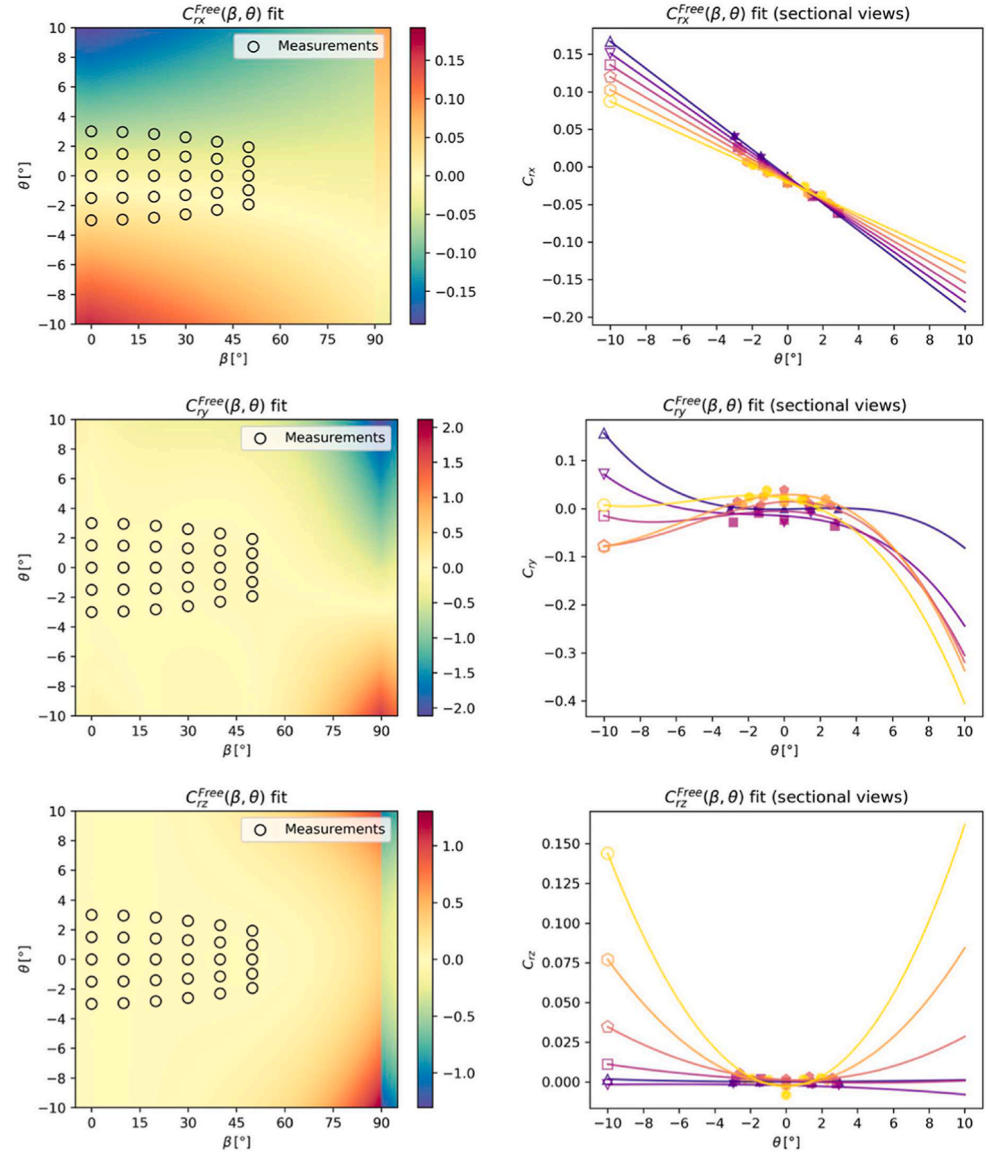

R^2 values of the n^{th} degree free polynomial fit						
Degree	C_x	C_y	C_z	C_{rx}	C_{ry}	C_{rz}
1	0.880	0.815	**0.990***	**0.991***	0.383	0.052
2	**0.962***	**0.969***	0.994	0.997	0.532	0.437
3	0.965	0.971	0.996	0.997	**0.728***	0.499
4	0.978	0.985	0.996	0.997	0.734	**0.648***
5	0.980	0.986	0.997	0.999	0.827	0.676
6	0.981	0.986	0.997	0.999	0.828	0.676

*Polynomial degree adopted

Fig. 14. (*continued*).

the bridge girder model around its longitudinal x axis, denoted as a rx rotation, to access the wind loading at different wind angles. For skew winds, the effects of such a rotation on the local wind angles are shown in Fig. 8. A rx rotation of the girder causes the y and z axes to rotate as well but, equivalently and for better illustration purposes, the mean wind vector is rotated instead in Fig. 8, as it is the relative angles between the mean wind and the structure that are of interest. Note that rx is directly correlated with θ_{yz}, with opposite sign, and not with θ. The mean wind vectors, before and after the rx rotation, are denoted $\boldsymbol{U}_{rx=0}$ and $\boldsymbol{U}$ respectively. Also, the yaw angle may change with rx, from an initial value $\beta_{rx=0}$ to β. From an initial unrotated position with $\theta = \theta_{yz} = 0°$ and with given values of $\beta_{rx=0}$ and rx, it is possible to estimate the resulting β, θ and θ_{yz} using eqs. (3)–(5), which are valid for $\beta_{rx=0} \in [-90°, 90°] \wedge rx \in [-90°, 90°]$.

$$\beta = \arctan\left(\frac{\tan(\beta_{rx=0})}{\cos(rx)}\right) \tag{3}$$

$$\theta = -\arcsin(\cos(\beta_{rx=0})\sin(rx)) \tag{4}$$

$$\theta_{yz} = -rx \tag{5}$$

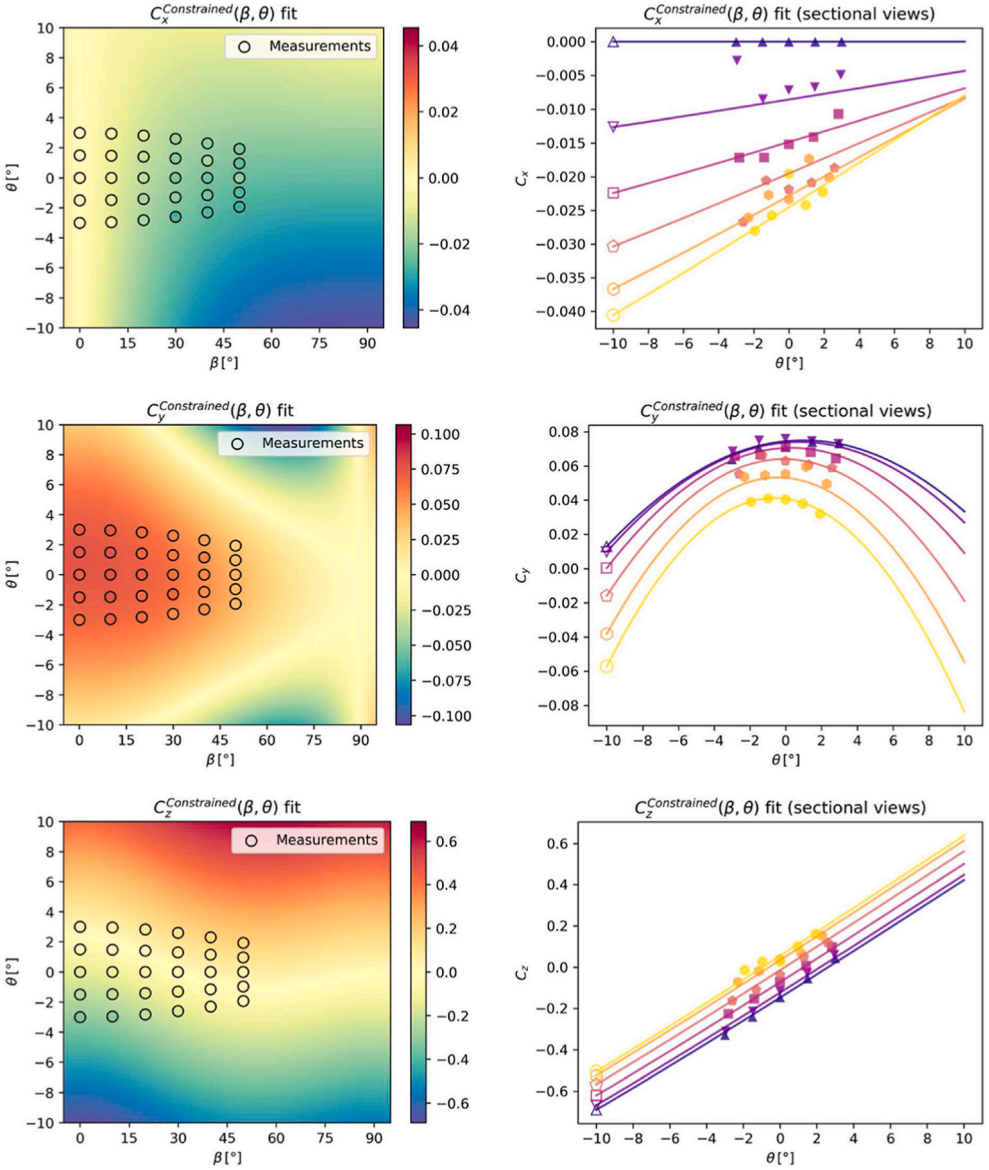

Fig. 15. Constrained bivariate polynomial fits of the aerodynamic coefficients.

Also, it may be helpful to obtain θ_{yz} from known values of β and θ, through eq. (6).

$$\theta_{yz} = \arcsin\left(\sin\theta \Big/ \sqrt{1-\sin^2\beta\cos^2\theta}\right) \tag{6}$$

In 2D analyses, i.e. with only the wind components in the normal plane, the aerodynamic loads are traditionally represented in the Drag, Lift and Moment directions. However, in 3D analyses, different representations of the wind forces have been used. In (Costa et al., 2022), representing the aerodynamic coefficients in the global wind system *Gw* $(\boldsymbol{X_u}, \boldsymbol{Y_v}, \boldsymbol{Z_w})$ achieves a more compact formulation of the buffeting and self-excited forces. However, in the present case study, the local structural system *Ls* $(\boldsymbol{x}, \boldsymbol{y}, z)$ is used to represent the aerodynamic coefficients, together with a normalization by the total mean wind speed squared U^2 and the cross-section width B (or B^2), such that the vector of mean aerodynamic forces per unit length in the *Ls* system $\boldsymbol{f}_{mean,Ls}$ is expressed by eq. (7).

$$\boldsymbol{f}_{mean,Ls} = 1 \Big/ 2\rho U^2 \boldsymbol{BC}_{Ls}(\beta,\theta) = 1 \Big/ 2\rho U^2 \begin{bmatrix} B & 0 & 0 & 0 & 0 & 0 \\ 0 & B & 0 & 0 & 0 & 0 \\ 0 & 0 & B & 0 & 0 & 0 \\ 0 & 0 & 0 & B^2 & 0 & 0 \\ 0 & 0 & 0 & 0 & B^2 & 0 \\ 0 & 0 & 0 & 0 & 0 & B^2 \end{bmatrix} \begin{bmatrix} C_x \\ C_y \\ C_z \\ C_{rx} \\ C_{ry} \\ C_{rz} \end{bmatrix}_{(\beta,\theta)} \tag{7}$$

Wind- and structure-based coordinate systems have their pros and cons, which should be weighted by the user. The *Ls* $(\boldsymbol{x},\boldsymbol{y},z)$ system representation was used here, with the following advantages:

1. It is consistent regardless of wind direction, avoiding transformations between instantaneous and mean wind directions when describing the static aerodynamic forces.
2. It is practical in both the experimental setup and the FEM implementation.
3. It enables intuitive and easily defined constraints on the polynomials for fitting the aerodynamic coefficients, as shown in Section 2.3.
4. It describes well the axial direction with $\boldsymbol{x}$ and $\boldsymbol{rx}$, as well as the perpendicular $(\boldsymbol{y})$ and vertical (z) directions, and it isolates the two

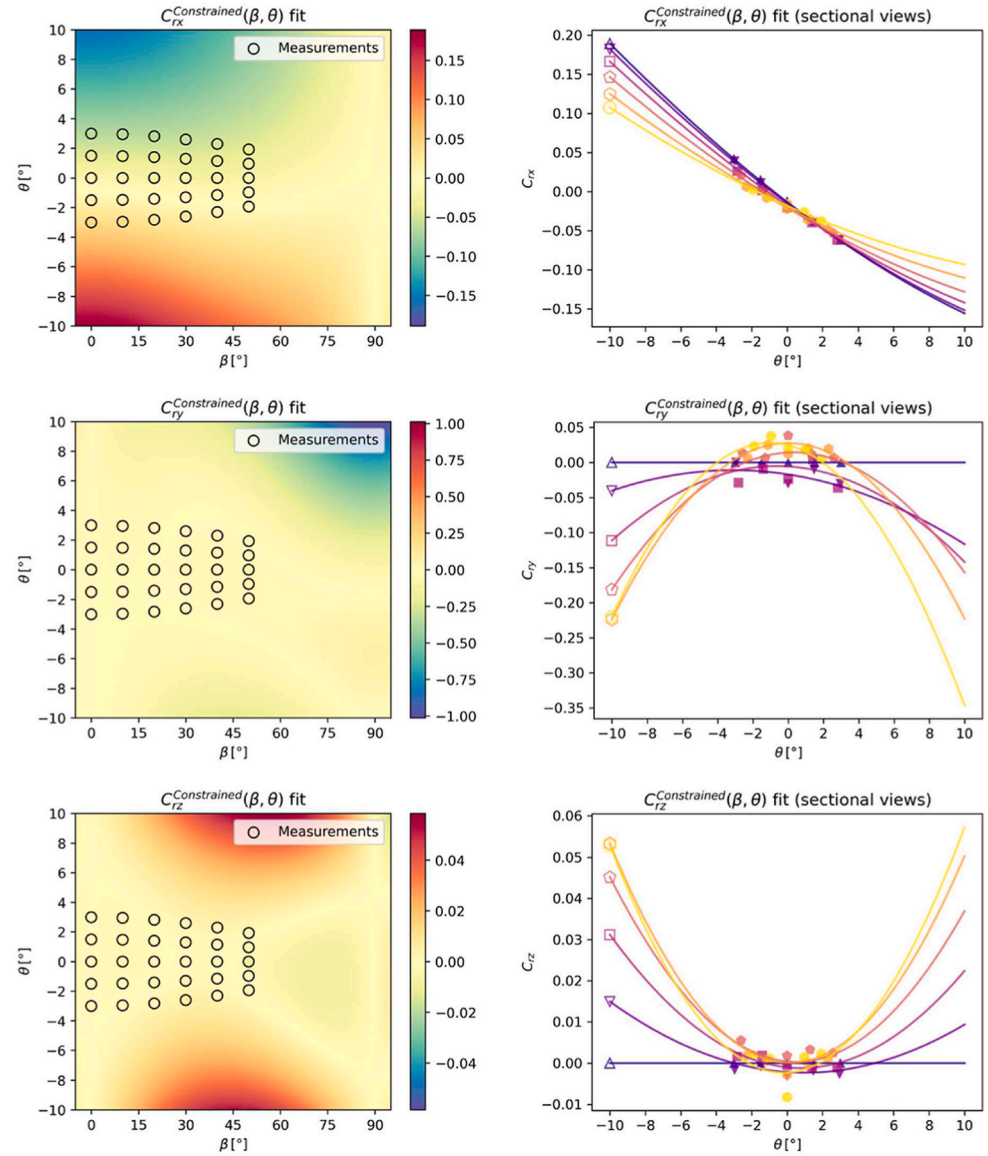

R^2 values of the n^{th} degree constrained polynomial fit						
Degree	C_x	C_y	C_z	C_{rx}	C_{ry}	C_{rz}
1	-2.55	-24.20	0.274	-0.331	-0.027	-0.003
2	0.888	-24.20	0.274	-0.331	0.168	0.021
3	**0.945***	0.758	0.766	0.939	0.479	0.073
4	0.960	**0.961***	**0.983***	**0.996***	**0.724***	**0.453***
5	0.975	0.967	0.983	0.996	0.727	0.536
6	0.979	0.968	0.982	0.996	0.802	0.665

*Polynomial degree adopted

Fig. 15. (*continued*).

often negligible coefficients C_{ry} and C_{rz}, as opposed to a wind-oriented coordinate system.

5. A normal-projection coordinate system representation (such as Drag, Moment and Lift) would lead to extra non-linearities due to the projections and it would be discontinuous at certain regions (e.g. at $\beta = \pm 90°$ an inversion of the normal drag direction occurs). Also, it is often associated with an inconsistent normalization (e.g. Drag normalized by H and Lift normalized by B) that could lead to mistakes in the transformations (and also lose meaning at large angles).

Note that when C_y is plotted as a function of θ, the plotted curve can concave downwards, contrary to the more traditional drag coefficient that usually concaves upwards for similar cross-sections (the reason for this is that the second derivative of C_y, evaluated at $\theta = 0$, depends on the slope of the Lift, the second derivative of the Drag, and the Drag itself, though this is not relevant for the analysis).

A mean wind speed of approximately 5 m/s was used in the experiments, together with a turbulent flow setting where horizontal and vertical turbulence intensities where measured at 10% and 7%, respectively. The static aerodynamic coefficients were obtained by

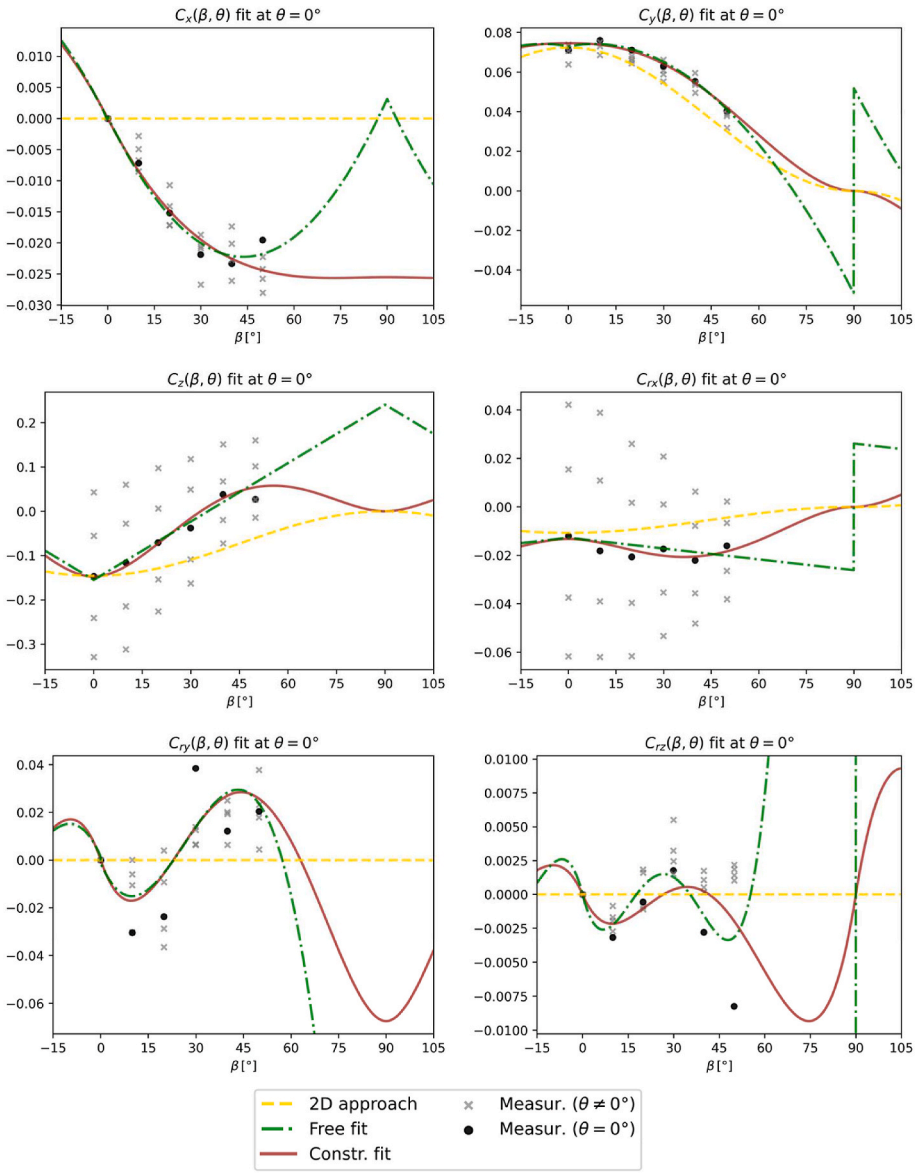

Fig. 16. Sectional view, at a fixed $\theta = 0°$, of the different fits of the aerodynamic coefficients.

averaging the measured forces over 60 s, at a 500 Hz sample rate, for each mean wind direction. A 6 DOF "*ATI Industrial Automation Mini45*" force/torque sensor was used.

The tests were conducted for six initial angles of $\beta_{rx=0}$ (0°, 9.90°, 19.90°, 29.90° and 39.90°) and, for each of them, five different rx rotations ($-$ 3.0°, $-$ 1,5°, 0°, 1.5° and 3.0°). The tested angles, expressed in β and θ, and the measured coefficients are presented in the Appendix.

The results from the wind tunnel tests need to be interpolated and extrapolated in order to be used in the buffeting analyses of the finite element model at different instantaneous values of $\widetilde{\beta}$ and $\widetilde{\theta}$ (variables represented with a tilde accent are time- and turbulence-dependent).

To assess the $\widetilde{\theta}$-interval of interest, 1 million samples of u, v and w were generated in Fig. 9, assuming them independent of each other, normally distributed, with $\sigma_i = I_i\, U$ obtained from Table 1, and with an arbitrary global (homogeneous) mean wind direction. The joint and marginal probability density functions of the instantaneous $\widetilde{\theta} = \arcsin(\widetilde{U}_z/\widetilde{U})$ and $\widetilde{\beta} = atan2(-\widetilde{U}_x/\widetilde{U}_y)$ are plotted, where $\widetilde{U} = \sqrt{(U+u)^2+v^2+w^2}$ and where $\widetilde{U}_x$, $\widetilde{U}_y$ and $\widetilde{U}_z$ are the local x, y and z components of $\widetilde{U}$. The yz-plane projection of the instantaneous inclination angle, $\widetilde{\theta}_{yz}$, is also included for reference. The 10th and 90th percentiles (P10 and P90) are included for both $\widetilde{\theta}$ and $\widetilde{\theta}_{yz}$.

The domain and variance of $\widetilde{\theta}_{yz}$ increase strongly as $\widetilde{\beta}$ approaches $\pm 90°$, as anticipated. On the other hand, the tested domain of θ $[-3°, 3°]$ covers 50.5% of all occurring $\widetilde{\theta}$-values. An interval of $[-10°, 10°]$ would cover 97.2% of the occurring $\widetilde{\theta}$-values and is the interval used to illustrate the aerodynamic coefficient fits in Section 2.3.

Lastly, it should be mentioned that alternative model test setups could be considered when studying very large yaw angles. A rotatable girder with elongated pseudo ends on a large rotary table in a large wind tunnel or the cantilevered setup presented in (Zhu et al., 2002b) are two possibilities. A strip section perpendicular to the x axis was tested, but an oblique strip section, aligned with the wind, could also be considered. Local flow effects caused by the small air gaps or eccentricities between the girder and the pseudo ends, were neglected. These effects were assessed in (Zhu et al., 2002b) and (Zhu, 2002), by estimating the six aerodynamic coefficients with different air gap alignments relative to the wind, using different oblique strips. Small differences were observed for some of the DOF ($\boldsymbol{X_u}$, $\boldsymbol{Z_w}$, $\boldsymbol{rX_u}$), and larger differences were observed

Table 2
Boundary constraints adopted for the polynomial fits $P(\beta,\theta)$ of each C_i.

No.	Constraint equation	C_x	C_y	C_z	C_{rx}	C_{ry}	C_{rz}
1	$P(0°,\theta) = 0$	X[a]				X[a]	X[a]
2	$P(90°,\theta) = 0$		X[b]		X[b]		X[b]
3	$P(90°,0°) = 0$		X[a,c]	X[a]	X[a,c]		X[b,c]
4	$P(\beta, -90°) = 0$	X[a]	X[b]		X[b]	X[a]	X[a]
5	$P(\beta,90°) = 0$	X[a]	X[b]		X[b]	X[a]	X[a]
6	$P(\beta, -90°) = -1.9$			X[d]			
7	$P(\beta,90°) = 1.9$			X[d]			
8	$\partial P/\partial\beta(0°,\theta) = 0$		X[e]	X[e]	X[e]		
9	$\partial P/\partial\beta(90°,\theta) = 0$	X[f]		X[f]		X[f]	
10	$\partial P/\partial\beta(90°, 0°) = 0$	X[c]	X[g]	X[c]	X[g]	X[c]	

X – adopted constraint.
[a] Required by symmetry, for any cross-section.
[b] Required by symmetry, for a cross-section with a vertical plane (xz) of symmetry.
[c] Redundant constraint since it is a subset of another applied constraint.
[d] Adopted by assuming that the cross-section grossly behaves as a flat plate at $\theta = \pm 90°$.
[e] Adopted due to: 1) symmetry (for any cross-section), and 2) assumption of smoothness (differentiability class C^1) at the current boundary.
[f] Same as [e], but only valid for a cross-section with a vertical plane of symmetry.
[g] Adopted by assuming that the independence principle is valid locally.

for the other DOF ($\boldsymbol{Y_v}, \boldsymbol{rY_v}, \boldsymbol{rZ_w}$) that were associated with smaller valued coefficients.

2.3. Approximations and fits of the aerodynamic coefficients $\boldsymbol{C}(\beta,\theta)$

2.3.1. Initial considerations

The basic mean wind load expressions for the different skew wind formulations, namely the 2D approach, the traditional "Cosine rule" which is a further simplification of the 2D approach (see Section 2.3.3 for more details), and the preferred 3D approach are recalled in eqs. (8)–(10).

$$f_{mean,i}^{2D} = \begin{cases} 1/2\rho \boldsymbol{B} U_{yz}{}^2 C_i(\beta = 0°, \theta_{yz}), \ for\ i = y,z,rx \\ 0, \ for\ i = x,ry,rz \end{cases} \tag{8}$$

$$f_{mean,i}^{Cosine\ rule} = \begin{cases} 1/2\rho \boldsymbol{B} U^2 \cos^2\beta C_i(\beta = 0°, \theta), \ for\ i = y,z,rx \\ 0, \ for\ i = x,ry,rz \end{cases} \tag{9}$$

$$f_{mean,i}^{3D} = 1 \Big/ 2\rho \boldsymbol{B} U^2 C_i(\beta,\theta), \ for\ i = x,y,z,rx,ry,rz \tag{10}$$

where θ_{yz} is defined in eq. (6) and U_{yz} in eq. (11).

$$U_{yz} = U\sqrt{1 - \sin^2\beta\cos^2\theta} \tag{11}$$

For comparison purposes, all coefficients can be re-normalized by $1/2\rho \boldsymbol{B} U^2$, as in the 3D approach. A direct comparison of the quantities $\boldsymbol{C}(\beta = 0°, \theta_{yz}) U_{yz}{}^2/U^2$, $\boldsymbol{C}(\beta = 0°,\theta)\cos^2\beta$ and $\boldsymbol{C}(\beta,\theta)$ is then possible, where the first two quantities are denoted $\boldsymbol{C}^{2D}(\beta,\theta)$ and $\boldsymbol{C}^{Cosine\ rule}(\beta,\theta)$, to distinguish them from the $\boldsymbol{C}(\beta,\theta)$ coefficients that were estimated in a skew wind configuration for the 3D approach. This is expressed in eqs. (12) and (13).

$$C_i^{2D}(\beta,\theta) = \begin{cases} C_i(\beta = 0°, \theta_{yz}) U_{yz}{}^2/U^2, \ for\ i = y,z,rx \\ 0, \ for\ i = x,ry,rz \end{cases} \tag{12}$$

$$C_i^{Cosine\ rule}(\beta,\theta) = \begin{cases} C_i(\beta = 0°, \theta)\cos^2\beta, \ for\ i = y,z,rx \\ 0, \ for\ i = x,ry,rz \end{cases} \tag{13}$$

Since no experimental data was yet available for $\beta \in [90°, 180°]$ at the current project phase, the present cross-section is assumed to have a vertical plane of symmetry (xz plane). Then, the extrapolation of the coefficient fits from $\beta \in [0°, 90°]$ to the desired domain of $\beta \in]-180°, 180°]$ is performed through the symmetry transformations described in eq. (14) and Fig. 10.

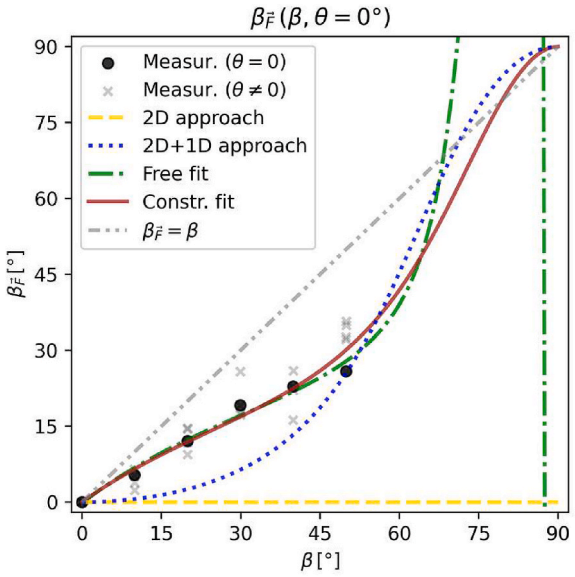

Fig. 17. Yaw angle of the mean resultant wind force $\beta_{\vec{F}}$ for different mean wind yaw angles β, at $\theta = 0°$.

$$\boldsymbol{C}_{Ls}(\beta,\theta) = \boldsymbol{T}_{sym}\boldsymbol{C}_{Ls}(\beta^*,\theta) \tag{14}$$

where β^* is the smallest angle between U_{xy} (mean wind projection onto the xy plane) and the y axis, such that $\beta^* \in [0°, 90°]$. β^* and $\boldsymbol{T}_{sym}$ are both given in Fig. 10, for different β-intervals.

The different polynomial fits to the experimentally obtained aerodynamic coefficients are now presented for the different skew wind load approaches. The coefficients of determination R^2 are included for the different polynomial degrees considered.

2.3.2. Comparing $\boldsymbol{C}^{2D}(\beta,\theta)$ with the measured $\boldsymbol{C}(\beta,\theta)$

In both the 2D approach and its Cosine rule approximation, only the five data points at $\beta = 0°$ are considered since these are the only available ones in a traditional wind tunnel test experiment with the mean wind normal to the girder. A univariate polynomial, as a function of θ, is fitted exclusively to these five points at $\beta = 0°$, using the least-squares method, for each coefficient, and extrapolated onto the β-dimension through eq. (12) and the β-dependencies of θ_{yz} and U_{yz}. A comparison between the resulting values $\boldsymbol{C}^{2D}(\beta,\theta)$ and the measured values $\boldsymbol{C}(\beta,\theta)$ is shown in Fig. 11. The calculated R^2 values, which include all the 30 data points, are a measure of the goodness-of-fit of such a simplified β-extrapolation that is implicitly assumed in a 2D buffeting load formulation.

As expected, the data points at $\beta = 0°$ are well fitted, but the poor fit at the remaining data points reinforces the idea that the 2D approach is a poor approximation of the actual three-dimensional wind flow and the corresponding skew wind load acting on a static bridge girder. Moreover, inconvenient discontinuities are obtained at $\beta = 90° \wedge \theta \neq 0$ for C_y and C_{rx} as a result of the yz projections in eq. (12) and the symmetry transformations.

2.3.3. Comparing $\boldsymbol{C}^{Cosine\ rule}(\beta,\theta)$ with the measured $\boldsymbol{C}(\beta,\theta)$

The Cosine rule is a further simplification of the 2D approach. It implicitly assumes that $U_{yz} \approx U\cos\beta$ and that $\theta_{yz} \approx \theta$. The adequacy of these approximations is investigated in Fig. 12.

The Cosine rule is seemingly identical to the 2D approach when $\theta = 0$, but even in $\theta = 0$ conditions, non-zero θ values need to be tested to e.g., estimate the derivatives of the aerodynamic coefficients. In the

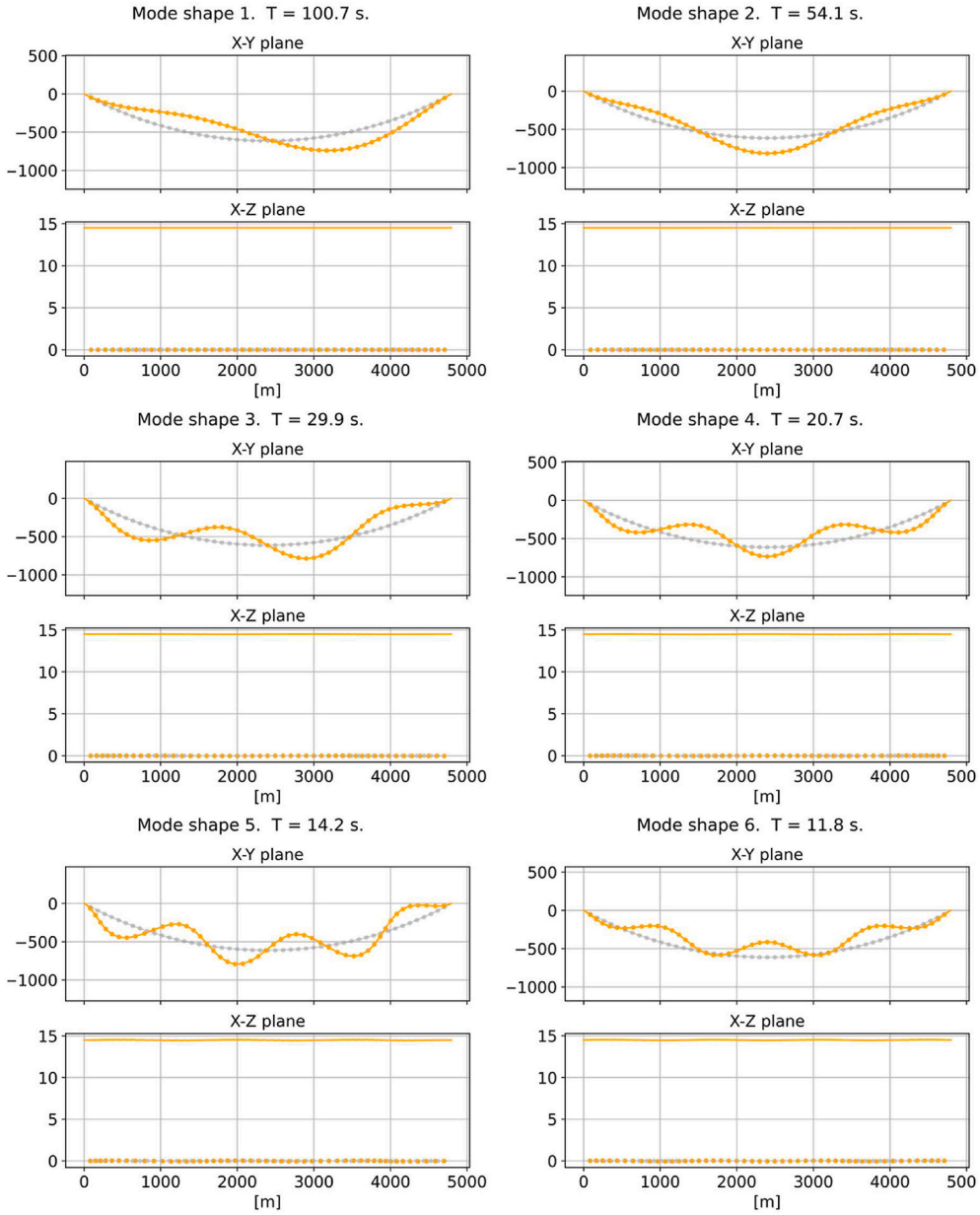

Fig. 18. Selected mode shapes of the simplified finite element model.

domain of the experimental data ($\beta \in [0°,50°] \wedge \theta \in [-3°,3°]$), both the 2D approach and its Cosine rule approximation give similar results, meaning that the experimental data is insufficient to compare both these approaches accurately. However, a "Cosine rule fit" is also included for comparison as it gives significantly different results beyond that domain. A univariate polynomial fit is first performed exclusively on the five data points at $\beta = 0°$, as in the 2D approach, followed by the extrapolation onto the β-dimension through $\cos^2\beta$, as in eq. (13). The resulting values $\boldsymbol{C}^{\textit{Cosine rule}}(\beta,\theta)$ and the measured values $\boldsymbol{C}(\beta,\theta)$ are compared in Fig. 13 and the R^2 values are provided.

Both the 2D approach and the Cosine rule give similar comparisons and similar R^2 values, as expected. One advantage of using the Cosine rule approximation is that it provides continuous and smooth coefficients throughout the domain as a consequence of using $\cos^2\beta$. On the other hand, the principle on which the Cosine rule is based (a wind projection onto the 2D normal plane) is not valid for large values of β and θ (as shown in Fig. 12).

2.3.4. *Bivariate polynomial fit to the measured* $\boldsymbol{C}(\beta,\theta)$

Bivariate (β,θ) polynomials are now used to fit the entire experimental dataset and later used as input for the 3D approach formulation. An example of a *maximum* 2nd degree polynomial is shown in eq. (15) (where e.g., a *total* 4th degree monomial $\beta^2\theta^2$ is allowed). Hereafter, "degree" refers to the highest degree used in the polynomial.

$$P(\beta,\theta) = c_{00} + c_{01}\theta + c_{02}\theta^2 + c_{10}\beta + c_{11}\beta\theta + c_{12}\beta\theta^2 + c_{20}\beta^2 + c_{21}\beta^2\theta + c_{22}\beta^2\theta^2 \tag{15}$$

The c constants are found with the least-squares solution, by minimizing $\sum_{k=1}^{m}\left(P_i(\beta_k,\theta_k) - C_i(\beta_k,\theta_k)\right)^2$, where k iterates over each of the m experimental data points of the aerodynamic coefficient C_i. It can be useful to reformulate the function to be minimized as $\sum_{k=1}^{m}(\boldsymbol{A}\boldsymbol{x}-\boldsymbol{b})_k^2$. The parameters $\boldsymbol{A}$, $\boldsymbol{x}$ and $\boldsymbol{b}$ are exemplified in eqs. (16)–(18), using the same 2nd degree polynomial example.

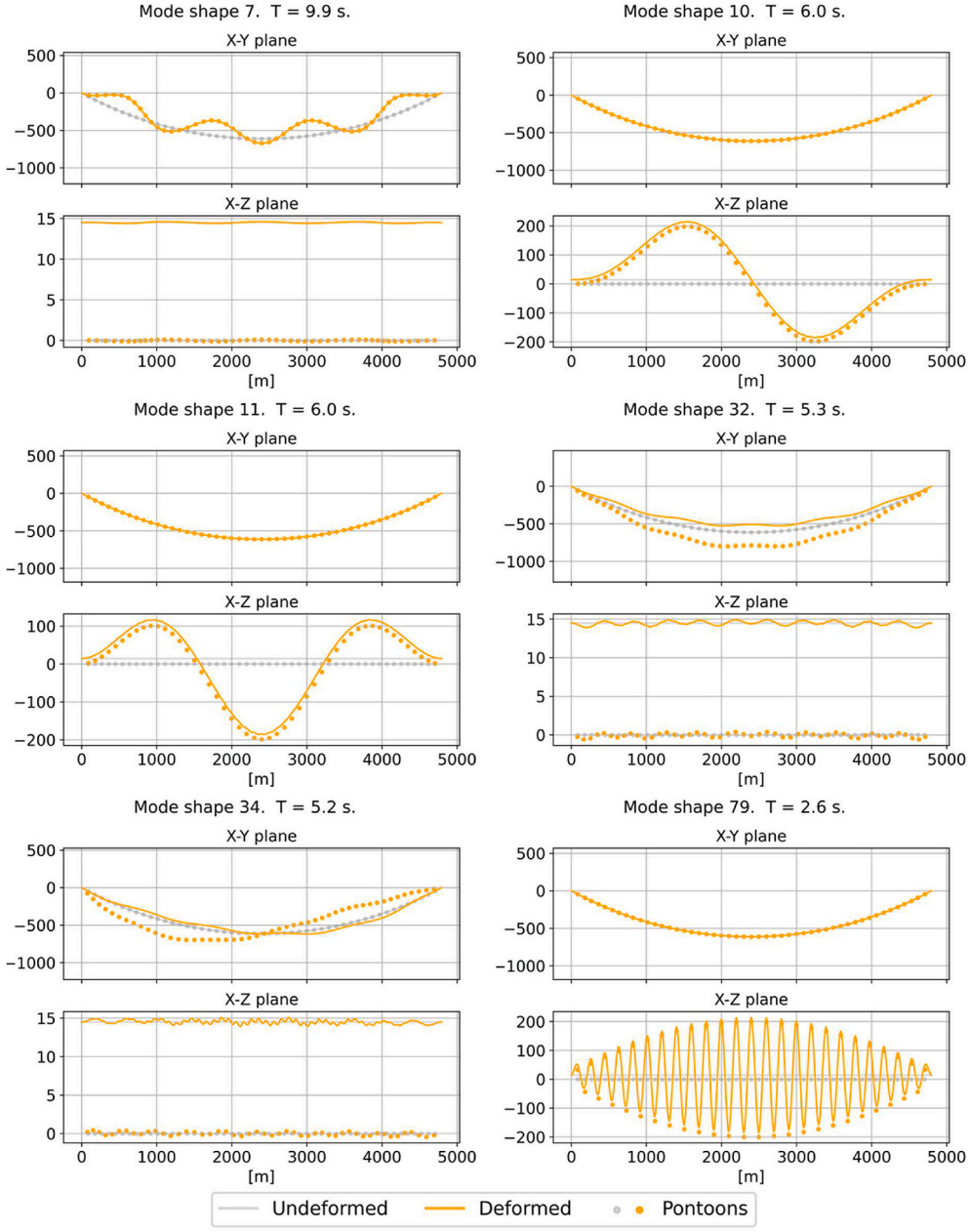

Fig. 18. (*continued*).

$$\boldsymbol{A} = \begin{bmatrix} 1 & \theta_1 & \theta_1^2 & \beta_1 & \beta_1\theta_1 & \beta_1\theta_1^2 & \beta_1^2 & \beta_1^2\theta_1 & \beta_1^2\theta_1^2 \\ \cdots & \cdots & \cdots & \cdots & \cdots & \cdots & \cdots & \cdots & \cdots \\ 1 & \theta_m & \theta_m^2 & \beta_m & \beta_m\theta_m & \beta_m\theta_m^2 & \beta_m^2 & \beta_m^2\theta_m & \beta_m^2\theta_m^2 \end{bmatrix} \tag{16}$$

$$\boldsymbol{x} = [\, c_{00} \quad c_{01} \quad c_{02} \quad c_{10} \quad c_{11} \quad c_{12} \quad c_{20} \quad c_{21} \quad c_{22} \,]^T \tag{17}$$

$$\boldsymbol{b} = [\, C_{i,1} \quad \cdots \quad C_{i,m} \,]^T \tag{18}$$

Then, the Jacobian row matrix of $\sum_{k=1}^{m} (\boldsymbol{Ax} - \boldsymbol{b})_k^2$ becomes simply $2(\boldsymbol{Ax} - \boldsymbol{b})^T\boldsymbol{A}$, and the Hessian matrix becomes $2\boldsymbol{A}^T\boldsymbol{A}$, which can be valuable inputs for an efficient minimization.

2.3.4.1. Free bivariate polynomial fits. In Fig. 14, free (unconstrained) polynomials are fitted to all six aerodynamic coefficients and compared with the measured values.

It is clear that bivariate polynomials provide good fits to the measurement data for the four main coefficients C_x, C_y, C_z and C_{rx}, even with low degree polynomials. The measured values of C_{ry} and C_{rz} are relatively small and irregular. The higher degree polynomials adopted for these two coefficients result in somewhat larger extrapolated values but their effect on the response is still small, as shown in Section 2.5.4.

One disadvantage of these free bivariate polynomials is that they provide discontinuous or non-differentiable results at the β-boundaries (see e.g. a discontinuity at $C_y(90°, \theta)$ or, less noticeably, of $\partial C_z/\partial\beta$ at $(0°, \theta)$ and $(90°, \theta)$, which is more clearly illustrated in Fig. 16). Also, due to the lack of data at higher values of β and θ, unrealistic values are estimated for some of the coefficients in these regions.

2.3.4.2. Constrained bivariate polynomial fits - the proposed fitting method. The present case study and buffeting analysis covers a large domain of yaw angles β from $-180°$ to $180°$ (and inclination angles θ from roughly $-10°$ to $10°$), which has only been partly covered by

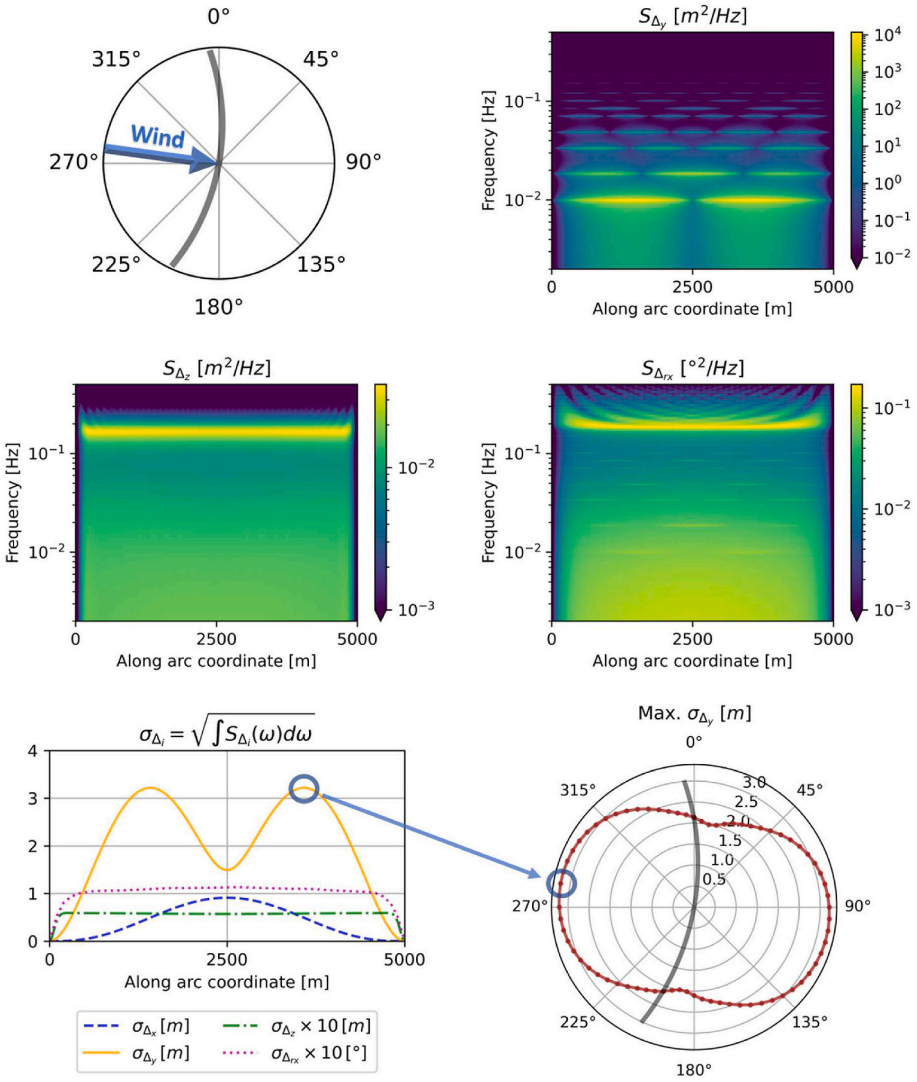

Figs. 19. 3D buffeting analysis example, in the frequency-domain, using constrained polynomial fits, for a mean wind cardinal direction $\beta_{Cardinal} = 280°$. Auto-spectral densities of the nodal displacement responses for ***y***, ***z***, and ***rx***. Standard deviation of the response along the bridge girder for ***x***, ***y***, ***z***, and ***rx***. Maximum standard deviation of the response in ***y***, for each global mean wind direction.

experimental data. This shortage of data is the first indication of a need to control the shape of the polynomials where no data is available, by imposing key physical principles at the boundaries. It should be noted that neither the present experiment nor previous literature has presented aerodynamic coefficients of bridge decks at yaw angles larger than 50°, and even if data was abundant, the aerodynamic coefficients $C(\beta, \theta)$ should still follow certain principles, such as continuity, differentiability and symmetry, in order to provide stable and reliable linearized numerical buffeting analyses. For example, simply mirroring a free polynomial fit from a tested domain (e.g. $\beta \in [0°, 90°]$) to an extrapolated domain (e.g. $\beta \in [90°, 180°]$) can compromise these principles. Hence, different shape constraints were introduced for different polynomial fits based on the expected aerodynamic behaviour at the boundaries of β and θ. Together with the symmetry transformations already introduced, these constraints enable smooth transitions of the fits at the boundaries (at $\beta = -90°$, 0°, 90° and ±180°), ensuring continuous and differentiable aerodynamic coefficients throughout the domain, as well as enforcing certain assumed polynomial shapes and encouraging the polynomials to remain within reasonable values. The boundary constraints adopted are presented in Table 2, for each fitted coefficient, within the domain $\beta \in [0°, 90°] \wedge \theta \in [-90°, 90°]$. They are considered valid for bridge section models with a constant cross-section along the ***x*** axis.

The two constraints marked with X^d (No. 6 and 7) prevent the polynomial fit from attaining extremely high or low values at the θ boundaries, which are very far from any data point. In the domain of interest, the polynomial is not sensitive to moderate variations around the chosen value of 1.9 (flat plate drag coefficient for $Re > 10^4$ according to (Veritas, 2010)). These two constraints lead to a higher linearity of C_z with respect to θ, in the θ-interval of interest, resembling the shape of C_z at $\beta = 0°$ of other comparable bridge cross-sections (such as the proposed Langenuen, Julsundet and new Sotra bridges) while still providing an accurate fit. The constraints marked with X^g can be explained in more detail, as follows:

A 2D approach, which assumes the independence principle, implies, for $\beta \in [0°, 90°]$, that:

- $C_y(\beta, \theta) \approx C_y(\beta = 0°, \theta_{yz}) {U_{yz}}^2 / U^2$
- $C_{rx}(\beta, \theta) \approx C_{rx}(\beta = 0°, \theta_{yz}) {U_{yz}}^2 / U^2$

Where θ_{yz} and U_{yz} are expressed in eqs. (6) and (11). Then, in the subdomain where $\beta = 90°$:

- $\partial({U_{yz}}^2 / U^2)/\partial\beta = 0$

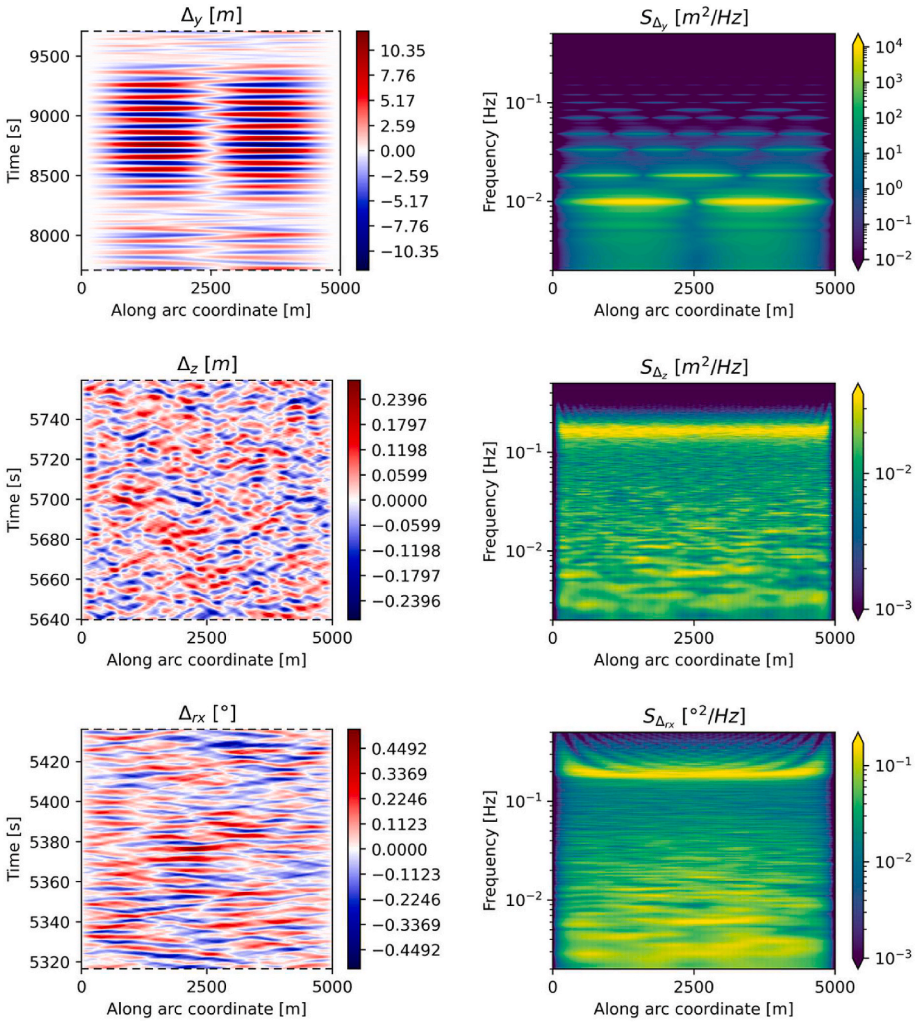

Fig. 20. Example of a 3 h time-domain simulation and respective spectral analysis of the response, for $\beta_{Cardinal} = 280°$. The time windows (left) are centred at the maximum obtained values, with a time range proportional to the relevant eigen modes depicted. The colour range of the spectra (right) is the same as in Fig. 19, for a direct comparison. (For interpretation of the references to colour in this figure legend, the reader is referred to the Web version of this article.)

And, at the point $\beta = 90° \wedge \theta = 0°$:

- $\partial\theta_{yz}/\partial\beta = 0$

This means that the polynomial fits of C_y and C_{rx} also comply with the constraint $\partial P/\partial\beta(90°, 0°) = 0$. This assumption aims to mitigate the data insufficiency at $\beta \approx 90°$ when other arguments (e.g., smoothness assumption) are not applicable. Note that $\partial\theta_{yz}/\partial\beta$ does not exist at $\beta = 90° \wedge \theta \neq 0°$.

Additionally, inequality constraints (e.g. $P(\beta, \theta) > 0$) could also be employed. Equality and inequality constraints can then be combined and fed into minimization algorithms to minimize the residual sum of squares already described. The Byrd and Omojokun's trust region algorithm was adopted, using *SciPy v1.6.1* (Virtanen et al., 2020), which is a toolbox available for *Python*. The software implementation of this algorithm is described in (Lalee et al., 1998)). Whenever the available tools are insufficient to automatically convert an inequality constraint on the polynomial into a system of inequalities of the polynomial coefficients (which is often the required format), the work by (Wahl and Espinasse, 2014) provides a useful procedure for some common constraints on multivariate polynomials.

The constrained polynomial fits are finally presented in Fig. 15. Constrained bivariate polynomials also provide good fits of the measurements for the four main coefficients C_x, C_y, C_z and C_{rx}. As expected, they provide continuous and smooth estimations, and constrain the results to reasonable values while preserving high R^2 values.

Particular attention is given to C_z and $\partial C_z/\partial\theta$ at high values of β, where no data is available to the authors' knowledge, and to the adopted constraints No. 6 and 7 (X[d]). A Cosine rule considers that $\partial C_z/\partial\theta = 0$ at $\beta = 90°$, which is a non-conservative assumption as any changes in $\widetilde{\theta}$ should lead to changes in the instantaneous vertical forces. This naturally affects the vertical response of the case studied at high yaw angles and is also deemed important for other bridges where the wind speed at high angles and the vertical turbulence are significant.

2.3.5. Additional comparisons

Some of the constraints and smoothness assumptions discussed can be better visualized in Fig. 16, where θ is fixed at $\theta = 0°$. The free polynomials are intentionally left out of the visible window for C_{ry} and C_{rz} where they attain disproportionally large values. Also, at $\theta = 0°$, there are no differences between the 2D approach and the Cosine rule so only the former is presented.

Next, the yaw angle of the resultant mean wind force $\beta_{\overrightarrow{F}}$ is plotted in Fig. 17 as a function of the mean wind yaw angle β, at a fixed inclination angle $\theta = 0°$, estimated from the different fits based on the measurements. This indicates whether the mean wind force is aligned with the mean wind $\boldsymbol{X_u Z_w}$ plane or not. The assumption of such a yaw alignment $\beta_{\overrightarrow{F}} = \beta$ (which could eventually be used in e.g. 2D CFD simulations that

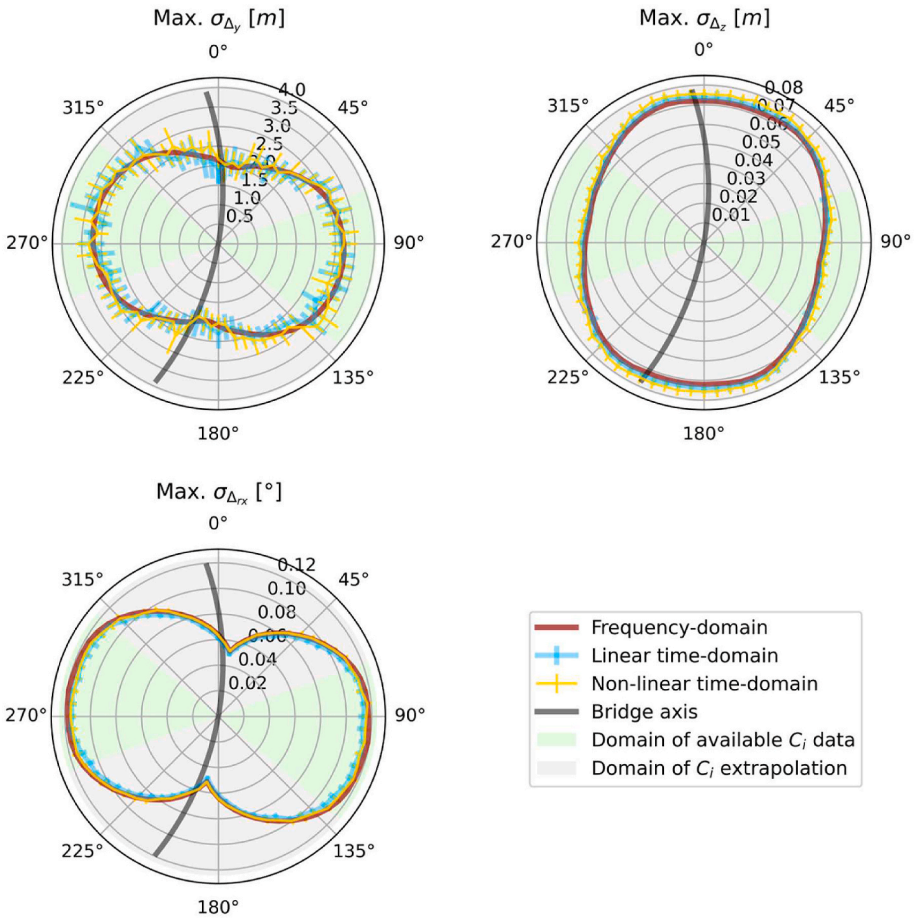

Fig. 21. Comparison between 3D frequency-domain and time-domain analyses (mean of 10 simulations, for each direction, whose standard deviation is indicated by the error bars). "Non-linear" refers to the use of aerodynamic coefficients as functions of instantaneous $\widetilde{\beta}$ and $\widetilde{\theta}$, instead of using a Taylor approximation.

are performed on oblique cross-sections coplanar with the wind $\boldsymbol{X_u Z_w}$ plane) is not recommended, since $\beta_{\overrightarrow{F}} \neq \beta$ for most yaw angles β.

2.4. Finite element model

A finite element model was assembled in *Python*, following conventional practices described in e.g. (Bathe, 2006; Clough and Penzien, 2003; Hutton, 2004). For the sake of simplicity and generality, the floating bridge is reduced to a 5000-m-long symmetric and horizontal Euler-Bernoulli beam with a constant curvature radius of 5000 m, at an altitude of 14.5 m, discretized every 25 m. The pontoons are modelled as nodes every 100 m at the water level with equivalent mass, damping and hydrostatic stiffness properties, including the frequency-dependent hydrodynamic added mass and potential damping, using the software *Ansys Aqwa 2019R1*. More information about these hydrodynamic loads (described in e.g. (Faltinsen, 1993)) can be found in (Norwegian Public Roads Administration, 2019d). The hydrodynamic interaction between pontoons, studied for the same bridge in (Xiang et al., 2018)), was not considered in this study. The pontoon nodes are connected to the girder via short and stiff columns. Structural damping was set to 0.5%, as Rayleigh damping, tuned to the two periods of 120 and 2 s.

The floating bridge studied has additional important damping sources, such as non-linear hydrodynamic viscous forces due the pontoons' response relative to the local sea current. To accurately consider these forces was left outside the scope of this study as it would further add complexity to the results and reduce their interpretability. The model is not intended for absolute assessments of the response but rather for relative assessments of the different load models.

The obtained mode shapes and eigen periods resemble those reported in the latest design reports (concept *K11* in e.g. (Norwegian Public Roads Administration, 2019a)). The mean wind forces significantly affect the first few mode periods of this particular structure. Mean wind directions that cause mean tension forces in the girder reduce these modes' eigen period, whereas mean wind directions that lead to mean compression forces increase it, due to geometric stiffness effects. For simplicity, static wind effects were not included in the analysis. A few key eigen modes are presented in Fig. 18 in the horizontal (***XY***) and vertical (***XZ***) planes, multiplied by a scale factor of 200 for visualization purposes. These are the first 7 horizontal modes, where mode 6 and 7 have a high axial participation, the first two vertical modes (modes 10 and 11) with nearly identical mode periods, the two first torsional modes (modes 32 and 34) and one of the last relevant vertical modes (mode 79) that still mobilizes the pontoons, meaning that most of the vertical response comes from a narrow band between the periods of 6.0 and 2.6 s.

2.5. Buffeting analysis

2.5.1. Methodology and validation

In the following sections, the established finite element model of the floating bridge is subjected to different skew wind buffeting load models. First, an illustrative example of the frequency-domain analysis performed, using the previously introduced constrained polynomial fits and the 3D approach, is shown in Fig. 19. The first 100 eigen modes were included in the analysis and the Complete Quadratic Combination (CQC) method was used. In this example, the mean wind cardinal direction $\beta_{Cardinal} = 280°$ is adopted, which corresponds to having $\beta = 180°$ at the middle of the bridge, as illustrated. A linearized 3D buffeting analysis

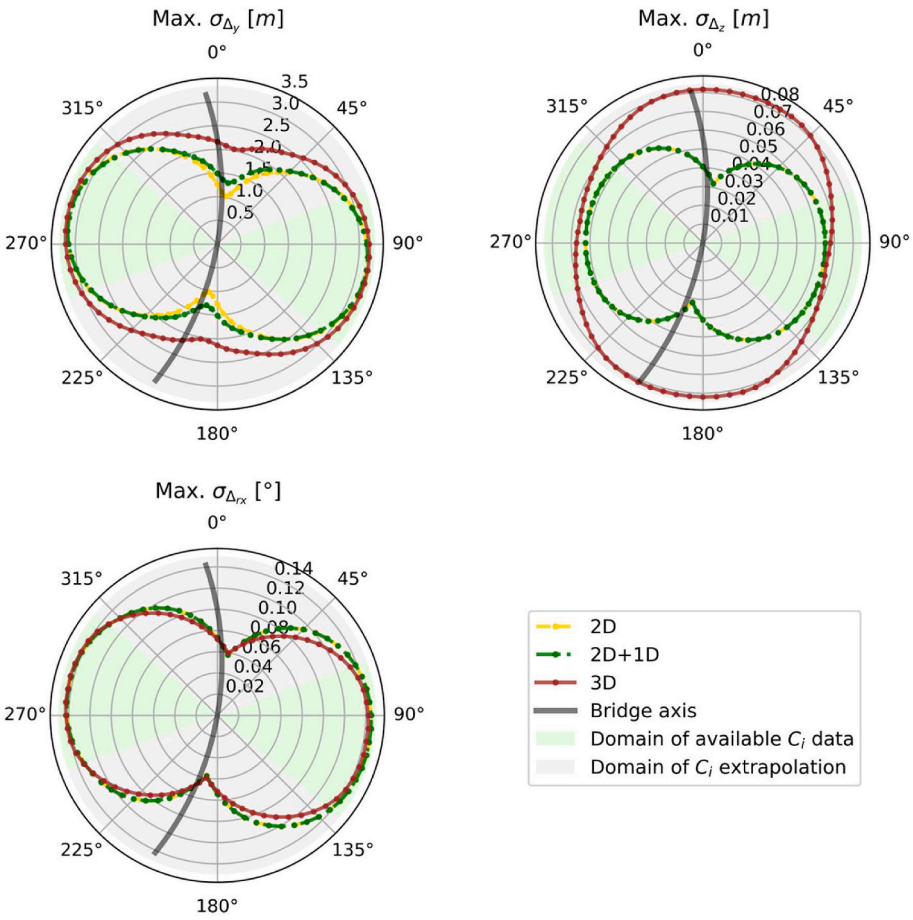

Fig. 22. Maximum bridge responses, for each mean wind direction, for different theoretical models of the skew wind buffeting. The same constrained polynomial fits of the aerodynamic coefficients are used.

then provides the auto-spectral densities of the nodal displacement response, shown for ***y***, ***z*** and ***rx***, at different positions along the bridge girder. The integrated response follows, also presented along the bridge girder. Then, by noting the maximum response values along the bridge, and iterating this process for all possible mean wind directions, a final polar plot of the maximum standard deviation σ_{Δ_i} of the relevant response components can be presented, providing an overview of the bridge behaviour for all mean wind directions.

Time-domain simulations of the wind field and the structural response are also implemented as a tool to validate the results of the frequency-domain simulations. In both the time- and frequency-domain analyses that are being compared in this section, the frequency-dependent added mass and damping were set at fixed frequency values corresponding to the dominant eigen frequencies of each DOF, for simplicity and to improve computational efficiency, with reasonable accuracy. These frequency dependencies are fully accounted in the following sections 2.5.2 to 2.5.5, where only computationally efficient frequency-domain analyses are performed. A representative example of one 3 h long simulation is illustrated in Fig. 20, for the same mean wind direction $\beta_{Cardinal} = 280°$. A time step of 0.25 s was used. The time windows plotted (left side) are centred at the maximum obtained Δ_i values during the simulation and show a time range proportional to the relevant eigen modes depicted. The respective spectral analyses (right side) of the time-domain response reflect the entire 3 h simulation, which starts after an initial 20 min transient period, with colour ranges matching those from the frequency-domain for a direct comparison. There is an apparent similarity between the spectral response in the frequency-domain and the spectral analysis of the time-domain response in the example given, supporting their validity.

Next, ten different time-domain simulations are performed for each global mean wind direction. The mean values and standard deviations (by using error bars) of all ten simulations' maximum responses are noted and plotted in Fig. 21 for each direction, where a comparison is made with the frequency-domain results. Additionally, the assumption of linearized coefficients, i.e., $\widetilde{C}(\widetilde{\beta},\widetilde{\theta}) \approx C(\beta,\theta) + C'^{\beta}(\beta,\theta)\Delta\beta + C'^{\theta}(\beta,\theta)\Delta\theta$, is also assessed in the time-domain where instantaneous $\widetilde{\beta}$ and $\widetilde{\theta}$ are easily obtained at each time step. The two different types of analyses and the linear and non-linear coefficient formulations provide reasonably similar results.

A series of sensitivity studies were also conducted to ensure convergence of the present model results. Some of the parameters studied include the different frequency discretizations, number of modes included, number of nodes, time step, simulation duration and transient period duration.

The effects of the admittance functions are conservatively disregarded in this study. These effects could be relevant for the higher vertical and torsional modes, whereas, for the first horizontal mode, the wavelength of the relevant turbulence components (U/f) is roughly 100 times the cross-section width and thus the effect should be negligible. The wind has a major role on the horizontal response of this bridge, but the vertical and torsional responses are dominated by wave loads, which are not considered in this study.

In the following sections, various findings of the skew wind buffeting analyses performed are presented.

2.5.2. *Comparing the different skew wind buffeting formulations*

The 2D, 2D + 1D and 3D buffeting formulations are compared in Fig. 22, in terms of maximum response obtained. The same constrained

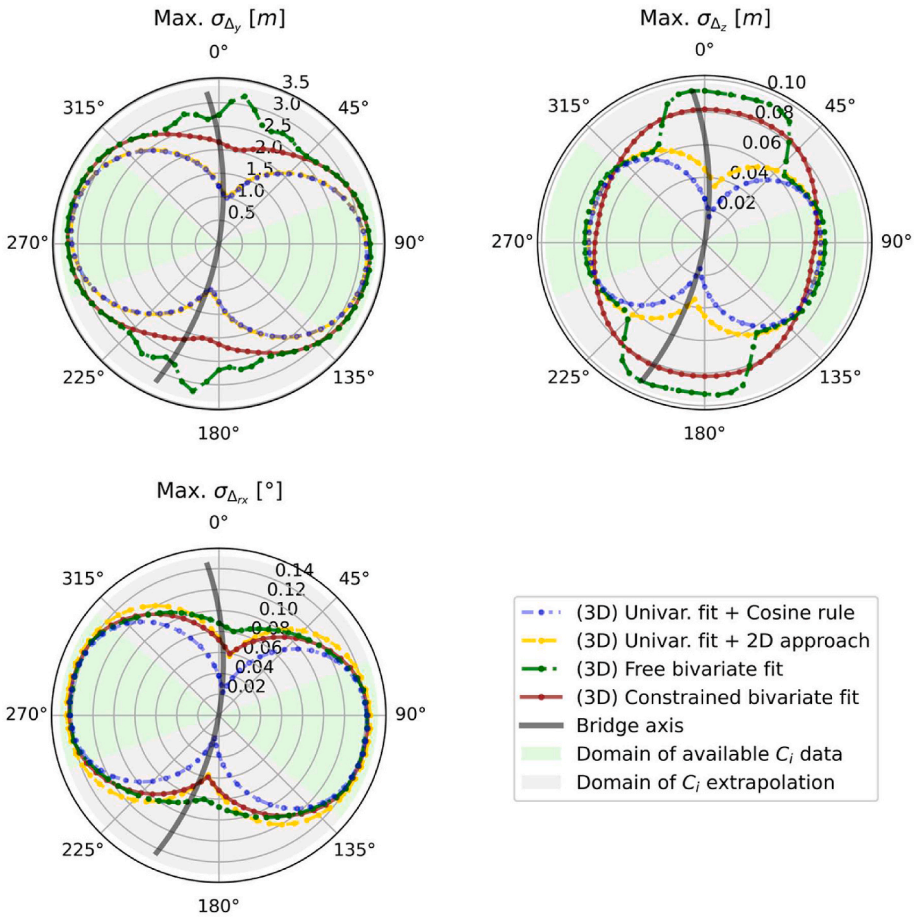

Fig. 23. Maximum bridge responses, for each mean wind direction, for different aerodynamic coefficient fitting methods. The 3D buffeting load formulation is used.

polynomial fits are used in all three cases in order to keep the focus on the different buffeting formulations. Note that only the 3D approach can use the data at $\beta \neq 0°$, except for the 2D + 1D formulation which simply imports the estimated value of C_x at $\beta = 90° \wedge \theta = 0°$ and additionally considers the wind projection onto the x axis. The maximum x axis response is omitted in the following plots as it closely resembles the shape of the maximum y axis response, only with smaller amplitudes.

Despite the inherent uncertainty of the C_i coefficients at large yaw angles, it is clear that there are important differences between the response estimates of the different buffeting load formulations. The vertical response, in particular, can be strikingly different. In the 3D approach, the maximum vertical response is estimated to occur at high yaw angles, and a large vertical response is observed on a wide range of yaw angles. These results require validation through more extensive wind tunnel tests, but it seems plausible that small changes in $\widetilde{\theta}$ can lead to changes in the vertical forces with similar (or perhaps larger) importance for large β as for small β. In other words, it seems plausible that $C_z'^{\theta}(0°, 0°) \approx C_z'^{\theta}(90°, 0°)$ despite that the latter one often goes unnoticed in literature and design practices. Also, it might be interesting to investigate the vertical response at large yaw angles in bridges with a significant vertical curvature of the deck, which would be overlooked using a Cosine rule approach. In Fig. 22, it can also be seen that adding the axial dimension (+1D) to the 2D approach affects the horizontal response at large yaw angles.

2.5.3. Comparing the different aerodynamic coefficient fitting methods

The maximum bridge response, for the different fitting methods previously introduced, is shown in Fig. 23. The 3D approach formulation is used in all four cases to draw out how the choice of a fitting method affects the response.

The main differences between the fitted coefficients of the "Univariate fit + Cosine rule" and the "Univariate fit + 2D approach" are found at large yaw angles β and at $\theta \neq 0°$, which thus affects the coefficients' partial θ derivatives at $\theta = 0°$. The impact of such differences in the horizontal response is only up to 3%, but they can be larger than 100% for the vertical and torsional responses. This is the first attempt in the literature to suggest that the Cosine rule should be replaced by the 2D approach, when experimental data is only available at $\beta = 0°$, since the 2D approach is seemingly more conservative and closer to the 3D bivariate estimates that utilize the data at $\beta \neq 0°$. For a straight and non-horizontal bridge girder, larger differences could be obtained. As for the preferred bivariate approaches, significant deviations are also obtained as expected, directly related to the fitting differences already discussed in Section 2.3. For the reasons already explained there, the constrained fit is believed to give the most reliable results. The important differences between the univariate and the bivariate polynomial fitting models are closely related to the 2D and 3D differences shown in Fig. 22. But note that introducing new data points to a polynomial fit can change the entire fit. This effect was suppressed in Fig. 22, where all approaches purposedly used the same constrained polynomial fits, for comparison, but it is naturally included in Fig. 23 (each univariate fit considered only the 5 data points at $\beta = 0°$, whereas each bivariate fit considered all 30 data points).

2.5.4. Comparing different aerodynamic coefficients' contributions to the response

The next step in the analysis is to assess the isolated effects of including the axial coefficient C_x as well as the two last rotational coefficients C_{ry} and C_{rz}, by using the 3D approach and the constrained

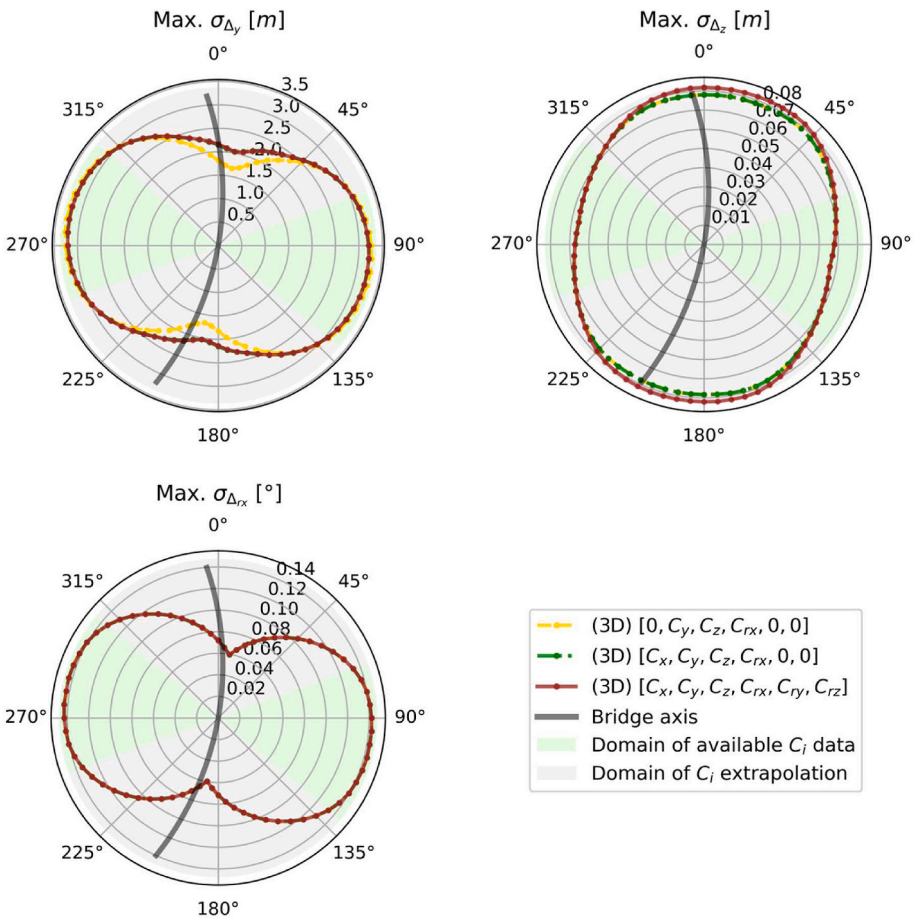

Fig. 24. Maximum bridge responses, for each mean wind direction, considering (or not) C_x, C_{ry} and C_{rz}. The 3D buffeting load formulation is used together with constrained polynomial fits.

polynomial fits for all three cases. The results are shown in Fig. 24. As expected, the axial coefficient C_x contributes to the horizontal response at large yaw angles, which is also a consequence of having a curved bridge. On the other hand, the effects of including the C_{ry} and C_{rz} coefficients seem relatively small despite the uncertainty from the poor fits obtained. The minor effects of C_{ry}, which mostly affect the vertical response, can be detected in the vertical response plot, at large yaw angles. The C_{rz}, which should mostly affect the horizontal response, has practically unnoticeable effects there.

2.5.5. Comparing the different skew wind quasi-steady motion-dependent force formulations

In this section, the effects of including the quasi-steady (QS) self-excited forces are investigated. Since the unsteady flutter derivatives under skew winds were not available for the case studied, the quasi-steady theory was assumed to be a sufficient approximation, given the low eigen frequencies and high mean wind speeds. This approximation should be investigated in a future study.

Three different QS formulations of the self-excited forces are compared in Fig. 25. "(QS) Zhu" is the formulation introduced in (Zhu, 2002). "(QS) Costa et al. (6 DOF)" is the formulation later proposed in (Costa et al., 2022) which considers all six degrees-of-freedom, further improved the aerodynamic stiffness terms and made a minor correction to the P_5^* term. The alternative "(QS) Costa et al. (3 DOF)" formulation is the same as the "(QS) Costa et al. (6 DOF)" formulation when only the three main DOF, namely $\boldsymbol{y}$, z and $\boldsymbol{rx}$, are considered, as in (Scanlan and Tomo, 1971).

It is noted that neglecting the quasi-steady self-excited forces changes the response substantially, particularly the horizontal response, which would be increased between 60% and 120%. These motion-dependent forces are an important source of damping for the first eigen modes where the hydrodynamic potential damping is very low. The vertical and torsional responses also see a significant increase, between 7% and 10%. For this case study, the three different formulations of the quasi-steady self-excited forces provide similar results. The "(QS) Zhu" and "(QS) Costa et al. (3 DOF)" formulations provide virtually the same results (less than 0.1% differences). The recommended "(QS) Costa et al. (6 DOF)" formulation is also similar, with differences up to 2.5% for the horizontal response, up to 1% for the vertical response and smaller than 0.1% for the torsional response.

3. Conclusions

One proposed floating bridge solution to cross the Bjørnafjord, in Norway, was modelled through a simplified finite element model. It is important to carefully investigate this bridge buffeting response for all possible mean wind directions due to its curvature, its long eigen periods, the relatively open surroundings and also for fatigue considerations.

Wind tunnel tests of a section model of the bridge girder were analysed for different combinations of the mean wind yaw angle β and inclination angle θ. Some of the challenges faced in the wind tunnel testing and data interpretation are discussed. Static aerodynamic coefficients were obtained for all six DOF. Despite the domain of yaw angles tested (up to 50°) being larger than what is available in the current literature, it was still necessary to significantly extrapolate the results for a complete 360° assessment of the skew wind buffeting response. Thus, different extrapolation approaches are presented, using

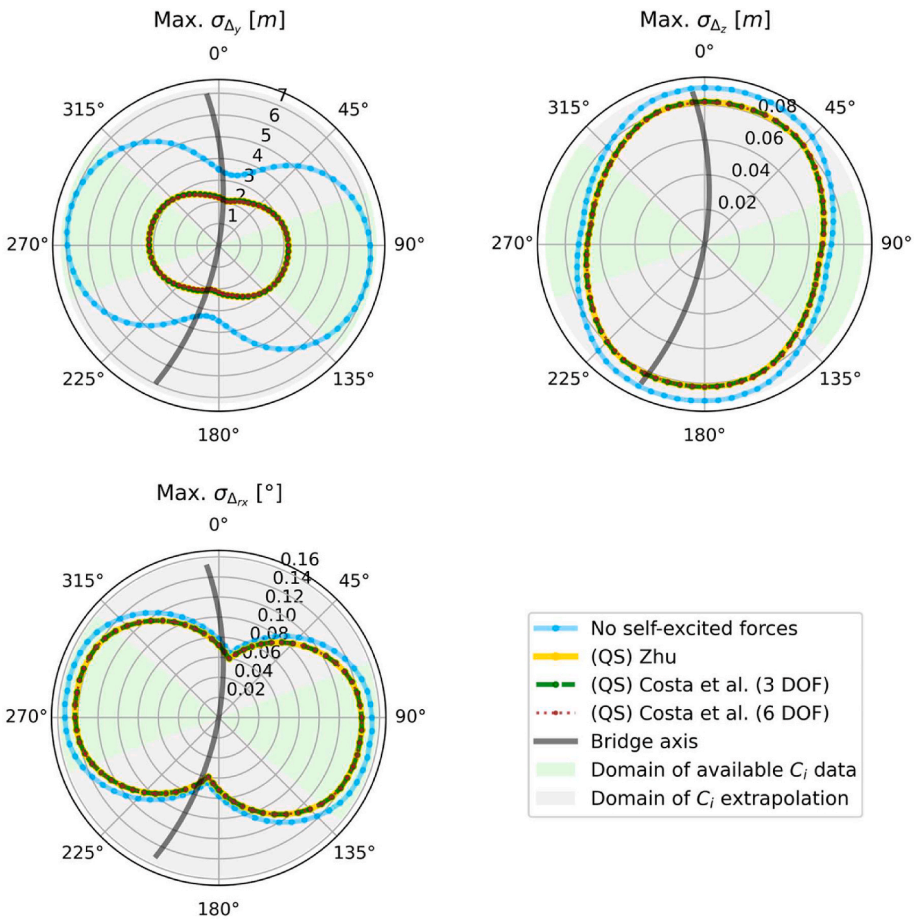

Fig. 25. Maximum bridge responses, for each mean wind direction, considering (or not) different formulations of the quasi-steady (QS) self-excited forces.

univariate and bivariate polynomial fits of the coefficients. Several possible constraints are investigated and applied to the bivariate polynomials, imposing key physical principles at the boundaries. The suggested constrained polynomials fit reasonably well the measured coefficients in the four main DOF, they provide sensible estimates in the challenging regions of β and θ that are far from the available data, and also, together with the appropriate symmetry transformations, they ensure smooth functions in the entire β and θ domain, as required by a linear approach.

Previously established theoretical models for the skew wind buffeting are grouped into so-called 2D, 2D + 1D and 3D approaches, depending on whether they only consider the wind components in the plane that is normal to the bridge girder (2D), additionally consider an independent axial component (+1D) or fully account for the three-dimensionality of the wind flow (3D). The present article provides the first comparison of these three methodologies. The three-dimensional wind field and the structural response were investigated in both frequency- and time-domain to increase confidence in the results.

The theoretical buffeting models and fitting methods that only consider the aerodynamic data at $\beta = 0°$ underestimated the response of the case studied at large yaw angles, relative to the models and methods that consider all the data. The large differences in the vertical response are particularly interesting, indicating a need for more comprehensive wind tunnel tests that can estimate $C_z^{'\theta}$ at large yaw angles. The traditional "Cosine rule" approximation of the 2D approach is believed to be particularly non-conservative at large yaw angles. Therefore, this work further consolidates the support for a 3D approach.

The bivariate aerodynamic coefficients are thought to be most conveniently represented in the local structural coordinate system. For the case studied, the axial coefficient C_x was of some importance at large yaw angles and should be included in the analyses. On the other hand, the rotational C_{ry} and C_{rz} coefficients were found to have a small impact on the response, with C_{rz} being particularly negligible.

Finally, three different quasi-steady formulations of the motion-dependent aerodynamic forces were compared, namely the original formulation by Le-Dong Zhu and the main and alternative formulations proposed in a preceding article (Costa et al., 2022). These self-excited forces have a large impact on the bridge response. However, the differences between the three different quasi-steady formulations are found to be smaller than 2.5% for this particular case study.

4. Recommendations for further work

A few recommendations for further work are summarized below:

- Wind tunnel tests could be performed for a larger domain of yaw and inclinations angles to better extrapolate the aerodynamic coefficients and more accurately compare the different fitting methods.
- The effects of non-homogeneity and non-stationarity of the mean wind speeds, mean wind directions, turbulence intensities, spectral properties and coherences properties could be investigated due to the large dimensions and very long eigen periods of the bridge studied.
- Different formulations of the normalized co-spectra of the wind turbulence could be pursued and their effects on the response compared. A non-zero spectral density between different wind components (e.g., S_{uw}), should also be considered.
- The axial coefficient C_x could be further improved to consider other bridge equipment (besides the railings) and to consider design cases where the wind loads and traffic are concomitant, such that the cumulative effect of many fast-moving vehicles against the wind is

considered for such long and continuous bridge girders as the one presented.

- An accurate estimation of the aerodynamic admittance functions, which were conservatively disregarded in this study, could be pursued, with a possible impact on the buffeting analysis, in particular for the vertical and torsional responses.
- Unsteady flutter derivatives under skew winds should provide more accurate motion-dependent forces. They could be estimated and compared with the quasi-steady formulation used. They have been previously estimated in (Zhu et al., 2002a). In the same study, an approximate method by (Scanlan, 1999), requiring only the unsteady flutter derivatives under normal wind, was included for comparison. The method by Scanlan was decreasingly accurate with increasing wind speeds. A hybrid method could also be pursued using Scanlan's method and imposing quasi-steady asymptotes at larger values of reduced wind velocities and yaw angles.

CRediT authorship contribution statement

Bernardo Morais da Costa: Conceptualization, Methodology, Software, Validation, Formal analysis, Investigation, Data curation, Writing – original draft, Writing – review & editing, Visualization, Project administration, Funding acquisition. **Jungao Wang:** Conceptualization, Validation, Data curation, Writing – review & editing, Supervision, Project administration, Funding acquisition. **Jasna Bogunović Jakobsen:** Conceptualization, Validation, Writing – review & editing, Supervision, Project administration, Funding acquisition. **Ole Andre Øiseth:** Conceptualization, Writing – review & editing. **Jónas Þór Snæbjörnsson:** Conceptualization, Writing – review & editing.

Declaration of competing interest

The authors declare that they have no known competing financial interests or personal relationships that could have appeared to influence the work reported in this paper.

Acknowledgements

The authors gratefully acknowledge the Norwegian Public Roads Administration, for the general research support within the innovative E39 Coastal Highway Route project, as well as The Research Council of Norway. This study was financially supported by both these organizations. The University of Stavanger is also acknowledged for their overall support. Svend Ole Hansen ApS is credited for conducting the wind tunnel experiments.

Appendix. Wind tunnel test results

Table A 1
30 tested pairs of angles (β, θ) in degrees.

(0.00, 3.00)	(9.91, 2.96)	(19.93, 2.82)	(29.93, 2.60)	(39.94, 2.30)	(49.94, 1.93)
(0.00, 1.50)	(9.90, 1.48)	(19.91, 1.41)	(29.91, 1.30)	(39.91, 1.15)	(49.91, 0.97)
(0.00, 0.00)	(9.90, 0.00)	(19.90, 0.00)	(29.90, 0.00)	(39.90, 0.00)	(49.90, 0.00)
(0.00, −1.50)	(9.90, −1.48)	(19.91, −1.41)	(29.91, −1.30)	(39.91, −1.15)	(49.91, −0.97)
(0.00, −3.00)	(9.91, −2.96)	(19.93, −2.82)	(29.93, −2.60)	(39.94, −2.30)	(49.94, −1.93)

Table A 2
Measured $C_x(\beta, \theta)$ with β and θ pairs from Table A. 1.

0.00E+2*	−4.91E-3	−1.07E-2	−1.87E-2	−2.01E-2	−2.22E-2
0.00E+2*	−6.75E-3	−1.41E-2	−2.09E-2	−1.73E-2	−2.42E-2
0.00E+2*	−7.18E-3	−1.52E-2	−2.19E-2	−2.33E-2	−1.95E-2
0.00E+2*	−8.53E-3	−1.71E-2	−2.06E-2	−2.27E-2	−2.58E-2
0.00E+2*	−2.82E-3	−1.72E-2	−2.67E-2	−2.61E-2	−2.80E-2

Table A 3
Measured $C_y(\beta, \theta)$ with β and θ pairs from Table A. 1.

7.32E-2	7.31E-2	6.45E-2	5.90E-2	4.95E-2	3.19E-2
7.40E-2	7.46E-2	6.81E-2	6.08E-2	5.95E-2	3.79E-2
7.11E-2	7.60E-2	7.11E-2	6.30E-2	5.53E-2	4.03E-2
7.07E-2	7.51E-2	6.67E-2	6.62E-2	5.45E-2	4.10E-2
6.39E-2	6.86E-2	6.57E-2	5.52E-2	5.35E-2	3.90E-2

Table A 4
Measured $C_z(\beta, \theta)$ with β and θ pairs from Table A. 1.

4.27E-2	5.99E-2	9.74E-2	1.18E-1	1.51E-1	1.60E-1
−5.51E-2	−2.79E-2	6.39E-3	4.88E-2	6.76E-2	1.02E-1
−1.47E-1	−1.16E-1	−7.03E-2	−3.75E-2	3.80E-2	2.74E-2
−2.41E-1	−2.15E-1	−1.54E-1	−1.09E-1	−1.95E-2	2.66E-2
−3.29E-1	−3.12E-1	−2.26E-1	−1.63E-1	−7.26E-2	−1.44E-2

Table A 5
Measured $C_{rx}(\beta,\theta)$ with β and θ pairs from Table A. 1.

-6.17E-2	−6.20E-2	−6.16E-2	−5.33E-2	−4.81E-2	−3.81E-2
−3.74E-2	−3.90E-2	−3.96E-2	−3.54E-2	−3.56E-2	−2.64E-2
−1.20E-2	−1.82E-2	−2.07E-2	−1.73E-2	−2.21E-2	−1.61E-2
1.55E-2	1.09E-2	1.75E-3	1.04E-3	−7.79E-3	−6.62E-3
4.22E-2	3.89E-2	2.61E-2	2.08E-2	6.35E-3	2.30E-3

Table A 6
Measured $C_{ry}(\beta,\theta)$ with β and θ pairs from Table A. 1.

0.00E+2*	−3.03E-2	−3.65E-2	6.58E-3	1.93E-2	4.44E-3
0.00E+2*	−1.05E-2	4.03E-3	1.26E-2	2.01E-2	1.79E-2
0.00E+2*	−3.05E-2	−2.38E-2	3.85E-2	1.22E-2	2.04E-2
0.00E+2*	−5.96E-3	−9.29E-3	6.38E-3	2.50E-2	3.78E-2
0.00E+2*	4.86E-5	−2.88E-2	1.39E-2	6.36E-3	2.32E-2

Table A 7
Measured $C_{rz}(\beta,\theta)$ with β and θ pairs from Table A. 1

0.00E+2*	−2.73E-3	−1.09E-3	2.46E-3	1.07E-3	2.19E-3
0.00E+2*	−1.94E-3	−8.82E-4	3.23E-3	1.62E-4	1.42E-3
0.00E+2*	−3.17E-3	−5.52E-4	1.78E-3	−2.80E-3	−8.24E-3
0.00E+2*	−8.42E-4	1.84E-3	1.51E-3	5.16E-4	1.03E-3
0.00E+2*	−1.69E-3	1.61E-3	5.51E-3	1.75E-3	1.87E-3

* Small, measured values marked with * were forced to 0 due to symmetry assumptions at $\beta = 0$.

References

Bathe, K.-J., 2006. Finite Element Procedures. Klaus-Jurgen Bathe.

Castellon, D.F., Fenerci, A., Øiseth, O., 2021. A comparative study of wind-induced dynamic response models of long-span bridges using artificial neural networks, support vector regression and buffeting theory. J. Wind Eng. Ind. Aerod. 209, 104484.

Cheynet, E., Jakobsen, J., Snæbjörnsson, J., Ágústsson, H., Harstveit, K., 2018. Complementary Use of Wind Lidars and Land-Based Met-Masts for Wind Measurements in a Wide Fjord, Journal of Physics: Conference Series. IOP Publishing, 012028.

Cheynet, E., Liu, S., Ong, M.C., Jakobsen, J.B., Snæbjörnsson, J., Gatin, I., 2020. The influence of terrain on the mean wind flow characteristics in a fjord. J. Wind Eng. Ind. Aerod. 205, 104331.

Clough, R.W., Penzien, J., 2003. Dynamics of Structures. Computers and Structures, Berkeley. CA.

Costa, B.M.d., Wang, J., Jakobsen, J.B., Øiseth, O.A., Snæbjörnsson, J.þ., 2022. Bridge buffeting by skew winds: a revised theory. J. Wind Eng. Ind. Aerod. 220, 104806.

Davenport, A.G., 1961a. The application of statistical concepts to the wind loading of structures. Proc. Inst. Civ. Eng. 19, 449–472.

Davenport, A.G., 1961b. The Spectrum of Horizontal Gustiness Near the Ground in High Winds.

Deodatis, G., 1996. Simulation of ergodic multivariate stochastic processes. J. Eng. Mech. 122, 778–787.

Di Paola, M., 1998. Digital simulation of wind field velocity. J. Wind Eng. Ind. Aerod. 74, 91–109.

Faltinsen, O., 1993. Sea Loads on Ships and Offshore Structures. Cambridge university press.

Hémon, P., Santi, F., 2003. Applications of biorthogonal decompositions in fluid–structure interactions. J. Fluid Struct. 17, 1123–1143.

Huang, M.-H., Lin, Y.-Y., Weng, M.-X., 2012. Flutter and buffeting analysis of bridges subjected to skew wind. J. Appl. Sci. Eng. 15, 401–413.

Hutton, D.V., 2004. Fundamentals of Finite Element Analysis. McGraw-hill.

Jian, B., Su, Y., Li, M., 2020. Buffeting response of cable-stayed bridge during construction under skew winds and pylon interference. KSCE J. Civ. Eng. 24, 2971–2979.

Kaimal, J.C., Wyngaard, J., Izumi, Y., Coté, O., 1972. Spectral characteristics of surface-layer turbulence. Q. J. R. Meteorol. Soc. 98, 563–589.

Kimura, K., Tanaka, H., 1992. Bridge buffeting due to wind with yaw angles. J. Wind Eng. Ind. Aerod. 42, 1309–1320.

Lalee, M., Nocedal, J., Plantenga, T., 1998. On the implementation of an algorithm for large-scale equality constrained optimization. SIAM J. Optim. 8, 682–706.

Li, S., Li, M., Zhang, L., 2016. Buffeting response of cable-stayed bridge under skew wind. In: Proceedings of the Advances in Civil, Environmental and Materials Research.

Midjiyawa, Z., Cheynet, E., Reuder, J., Ágústsson, H., Kvamsdal, T., 2021. Potential and challenges of wind measurements using met-masts in complex topography for bridge design: Part I–Integral flow characteristics. J. Wind Eng. Ind. Aerod., 104584

Norwegian Public Roads Administration, 2015. Handbook N400 for Bridge Design. https://www.vegvesen.no/fag/publikasjoner/handboker/.

Norwegian Public Roads Administration, 2018. Document: MetOcean Design Basis. Document no.: SBJ-01-C4-SVV-01-BA-001. https://hdl.handle.net/11250/2676915.

Norwegian Public Roads Administration, 2019a. Document: AMC Status 1 - Concept Evaluation. Appendix D - Initial Evaluations K11-K14. Document Code: 10205546-01-RAP-054 (limited access).

Norwegian Public Roads Administration, 2019b. Document: Concepts Definition and Description. Document no.: SBJ-32-C5-OON-22-RE-001 (limited access).

Norwegian Public Roads Administration, 2019c. Document: Preferred Solution, K12 – Appendix E – Aerodynamics. Document no.: SBJ-33-C5-AMC-20-RE-105. https://hdl.handle.net/11250/2659946.

Norwegian Public Roads Administration, 2019d. Document: Preferred Solution, K12 – Appendix F - Global Analyses - Modelling and Assumptions. Document No. SBJ-33-C5-AMC-90-RE-106. https://hdl.handle.net/11250/2660044.

Norwegian Public Roads Administration, 2019e. Document: Wind Model-Tests, Floating Bridge, Step 1, Small Scale Testing. Document No. SBJ-32-C4-SOH-20-RE-001. Rev 1. (limited access).

Øiseth, O., Rönnquist, A., Sigbjörnsson, R., 2013. Effects of co-spectral densities of atmospheric turbulence on the dynamic response of cable-supported bridges: a case study. J. Wind Eng. Ind. Aerod. 116, 83–93.

Olesen, H.R., Larsen, S.E., Højstrup, J., 1984. Modelling velocity spectra in the lower part of the planetary boundary layer. Boundary-Layer Meteorol. 29, 285–312.

Samferdselsdepartement, D., 2017. Meld. St. 33 Nasjonal Transportplan 2018–2029. Oslo, Norway.

Scanlan, R.H., 1999. Estimates of skew wind speeds for bridge flutter. J. Bridge Eng. 4, 95–98.

Scanlan, R.H., Tomo, J., 1971. Air Foil and Bridge Deck Flutter Derivatives. Journal of Soil Mechanics & Foundations Div.

Shinozuka, M., 1972. Monte Carlo solution of structural dynamics. Comput. Struct. 2, 855–874.

Tanaka, H., Davenport, A.G., 1982. Response of taut strip models to turbulent wind. J. Eng. Mech. Div. 108, 33–49.

Tao, T., Wang, H., Zhao, K., 2021. Efficient simulation of fully non-stationary random wind field based on reduced 2D hermite interpolation. Mech. Syst. Signal Process. 150, 107265.

Veritas, D.N., 2010. DNV-RP-C205 Recommended Practice Environmental Conditions and Environmental Loads.

Virtanen, P., Gommers, R., Oliphant, T.E., Haberland, M., Reddy, T., Cournapeau, D., Burovski, E., Peterson, P., Weckesser, W., Bright, J., 2020. SciPy 1.0: fundamental algorithms for scientific computing in Python. Nat. Methods 17, 261–272.
Wahl, F., Espinasse, T., 2014. Polynomial Regression under Shape Constraints.
Wang, H., Li, A., Hu, R., 2011. Comparison of ambient vibration response of the Runyang Suspension Bridge under skew winds with time-domain numerical predictions. J. Bridge Eng. 16, 513–526.
White, C.L., 2013. The State Route 520 Floating Bridge in Seattle. Washington. Proto-Type 1.
Xiang, X., Viuff, T., Leira, B., Øiseth, O., 2018. Impact of Hydrodynamic Interaction between Pontoons on Global Responses of a Long Floating Bridge under Wind Waves, International Conference on Offshore Mechanics and Arctic Engineering. American Society of Mechanical Engineers. V07AT06A049.
Xu, Y.L., Zhu, L.D., 2005. Buffeting response of long-span cable-supported bridges under skew winds. Part 2: case study. J. Sound Vib. 281, 675–697.
Zhou, Y., Sun, L., Xie, M., 2020. Wind characteristics at a long-span sea-crossing bridge site based on monitoring data. J. Low Freq. Noise Vib. Act. Control 39, 453–469.
Zhu, L.-D., 2002. Buffeting Response of Long Span Cable-Supported Bridges under Skew Winds: Field Measurement and Analysis. Department of Civil and Structural Engineering. Pao Yue-kong Library, The Hong Kong Polytechnic University, Hong Kong.
Zhu, L., Xu, Y., Xiang, H., 2002a. Tsing Ma bridge deck under skew winds—Part II: flutter derivatives. J. Wind Eng. Ind. Aerod. 90, 807–837.
Zhu, L., Xu, Y.L., Zhang, F., Xiang, H., 2002b. Tsing Ma bridge deck under skew winds—Part I: aerodynamic coefficients. J. Wind Eng. Ind. Aerod. 90, 781–805.
Zhu, L.D., Xu, Y.L., 2005. Buffeting response of long-span cable-supported bridges under skew winds. Part 1: Theory. J. Sound Vib. 281, 647–673.